



# Conditional Disorder in Small Heat-shock Proteins

T. Reid Alderson<sup>1,2</sup>, Jinfa Ying<sup>2</sup>, Ad Bax<sup>2</sup>, Justin L.P. Benesch<sup>1</sup> and Andrew J. Baldwin<sup>1,\*</sup>

**1** - Department of Chemistry, Physical and Theoretical Chemistry Laboratory, University of Oxford, South Parks Road, Oxford, OX1 3QZ, UK

**2** - Laboratory of Chemical Physics, National Institute of Diabetes and Digestive and Kidney Diseases, National Institutes of Health, Bethesda, MD, 20892, USA

Correspondence to Justin L.P. Benesch and Andrew J. Baldwin: [justin.benesch@chem.ox.ac.uk](mailto:justin.benesch@chem.ox.ac.uk), [andrew.baldwin@chem.ox.ac.uk](mailto:andrew.baldwin@chem.ox.ac.uk), [bax@nih.gov](mailto:bax@nih.gov)

<https://doi.org/10.1016/j.jmb.2020.02.003>

Edited by Sichun Yang

## Abstract

Small heat-shock proteins (sHSPs) are molecular chaperones that respond to cellular stresses to combat protein aggregation. HSP27 is a critical human sHSP that forms large, dynamic oligomers whose quaternary structures and chaperone activities depend on environmental factors. Upon exposure to cellular stresses, such as heat shock or acidosis, HSP27 oligomers can dissociate into dimers and monomers, which leads to significantly enhanced chaperone activity. The structured core of the protein, the  $\alpha$ -crystallin domain (ACD), forms dimers and can prevent the aggregation of substrate proteins to a similar degree as the full-length protein. When the ACD dimer dissociates into monomers, it partially unfolds and exhibits enhanced activity. Here, we used solution-state NMR spectroscopy to characterize the structure and dynamics of the HSP27 ACD monomer. We show that the monomer is stabilized at low pH and that its backbone chemical shifts,  $^{15}\text{N}$  relaxation rates, and  $^1\text{H}$ – $^{15}\text{N}$  residual dipolar couplings suggest structural changes and rapid motions in the region responsible for dimerization. By analyzing the solvent accessible and buried surface areas of sHSP structures in the context of a database of dimers that are known to dissociate into disordered monomers, we predict that ACD dimers from sHSPs across all kingdoms of life may partially unfold upon dissociation. We propose a general model in which conditional disorder—the partial unfolding of ACDs upon monomerization—is a common mechanism for sHSP activity.

© 2020 Elsevier Ltd. All rights reserved.

## Introduction

Small heat-shock proteins (sHSPs) comprise a class of ATP-independent molecular chaperones that are present in all kingdoms of life [1,2] and maintain cellular homeostasis by preventing the aggregation of partially unfolded or misfolded proteins [3,4]. In addition, human sHSPs play roles in regulating apoptosis and modulating the redox environment [5]. Given these essential biological roles, the dysregulation of sHSPs is implicated in cancer [6,7], cataract formation [8,9], and neurodegenerative diseases [10]. Moreover, disease-causing mutations in sHSPs have been directly linked to numerous myopathies, including Charcot-Marie-Tooth disease and distal hereditary motor neuropathy [11,12].

The amino-acid sequences of sHSPs, which themselves exhibit interesting physicochemical properties and contain significant amounts of intrinsic disorder [13–16], encode for dynamic structures that drive the diverse functionality of sHSPs. Typically, human sHSPs assemble into large, often heterogeneous oligomers that can respond to environmental cues [17,18]. Since the expression levels of numerous sHSPs are controlled by stress-inducible transcription factors [2], the oligomeric states of some sHSPs can be modulated by an increase in concentration upon stress-induced upregulation of expression. Moreover, changes in pH, temperature, oxidation state, and ionic strength can significantly increase or decrease the oligomeric size of sHSPs [19–23], and stress-induced activation of

signaling kinases that phosphorylate certain sHSPs can decompose the large oligomers into monomers and dimers [24,25]. The disassembly of some sHSPs into their constituent subunits has been shown to enhance their ability to protect against substrate aggregation [24,26,27], suggesting that competition between the binding of self and others may play a role in chaperone function.

The family of sHSPs is defined by an  $\alpha$ -crystallin domain (ACD) that comprises ~90 residues and

folds into an immunoglobulin-like  $\beta$ -sandwich [17]. ACDs readily dimerize with a low micromolar dissociation constant, and the organization of ACD dimers depends on the organism: metazoan ACDs dimerize through a long, anti-parallel  $\beta$ -sheet involving the  $\beta_6+\beta_7$  strand, whereas non-metazoan ACDs form domain-swapped dimers [17]. The ACDs of human sHSPs are generally flanked by disordered N- and C-terminal regions of low sequence conservation [14,15]. These regions vary in length

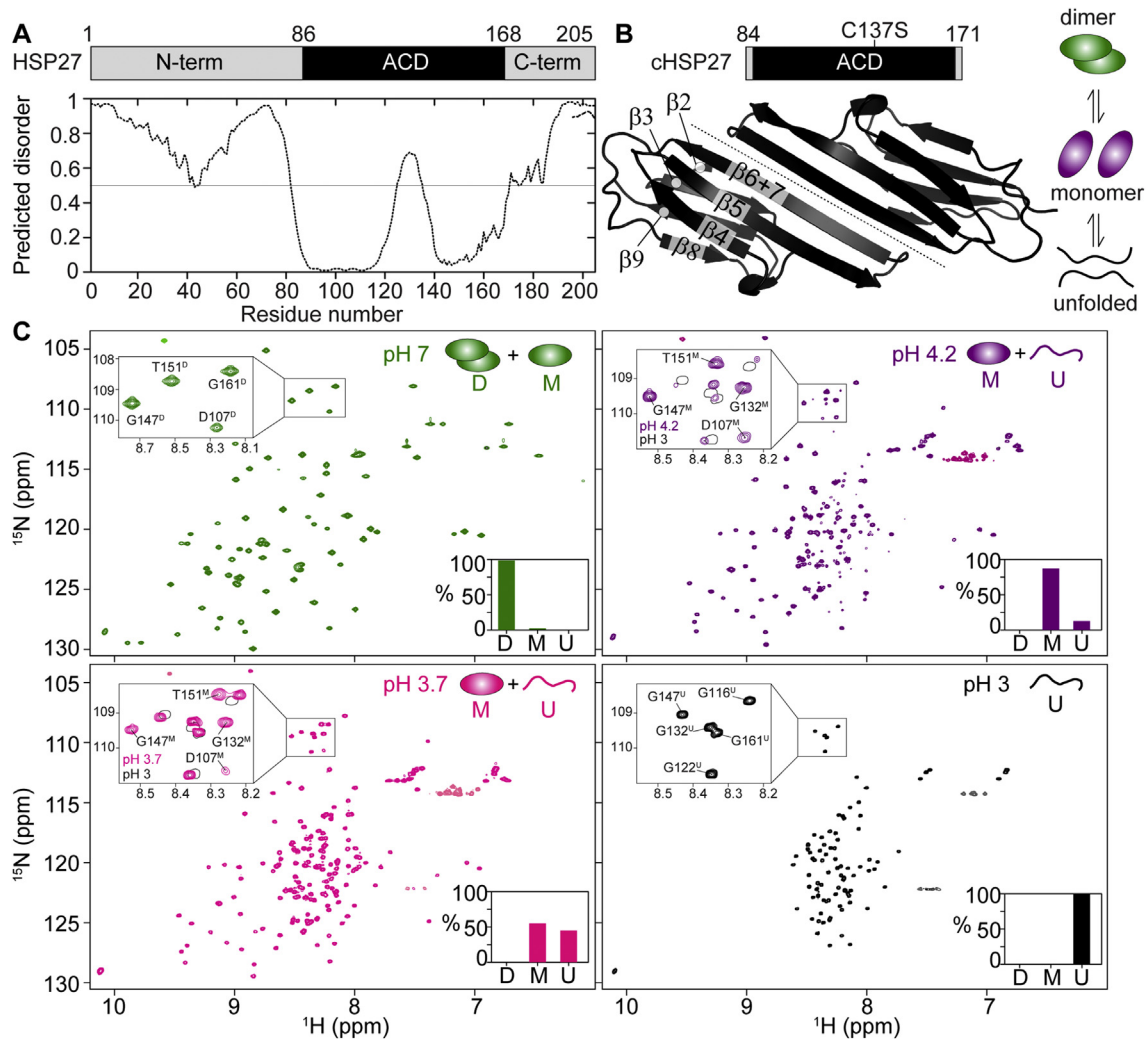


**Fig. 1.** Domain architecture of HSP27 and NMR spectra of its ACD in various states. (A) Linear domain depiction of HSP27 with numbers corresponding to domain boundaries. The predicted disorder based on the amino acid sequence is shown below, with values of 1 and 0 respectively corresponding to disordered and ordered. A horizontal line at 0.5 has been added for clarity. (B) *Top*: The cHSP27 construct contains the  $\alpha$ -crystallin domain with the C137S mutation to prevent disulfide bond formation. *Bottom*: crystal structure of the dimeric ACD (PDB: 4mjh) with the  $\beta$ -strands  $\beta_2$  through  $\beta_9$  indicated. *Right*: cHSP27 exists as a dimer (green), monomer (purple), and an unfolded form (black). (C) The equilibrium arrows in panel B are strongly affected by pH. 2D  $^1\text{H}$ - $^{15}\text{N}$  HSQC spectra of  $^2\text{H}$ ,  $^{13}\text{C}$ ,  $^{15}\text{N}$ -labeled cHSP27 as a function of pH. The percentage of dimer (D), monomer (M), and unfolded (U) is indicated in the lower-right of each spectrum. All spectra were recorded at 14.1 T and 25 °C and contoured at 10-fold the noise level (except panel D). Negative contours are shown in lighter colors in each spectrum. The insets depict a zoomed-in region. The single black contours in the pH 4.2 and 3.7 insets indicate the resonances from the pH 3 sample (unfolded).

among sHSPs but can exceed more than half of the total amino acid sequence, and their interactions with the ACD and other regions of sHSPs contribute to oligomerization [25,28,29]. Removal of both the N- and C-terminal regions prevents extensive oligomerization, and high-resolution structures have been determined for numerous isolated ACD dimers [30–33]. Human ACDs often retain the ability to prevent the aggregation of substrate proteins *in vitro* [26,31,34], indicating that functional features of sHSPs are encoded within this domain.

Among the 10 human sHSPs, HSP27 (HSPB1) is expressed in all tissues [2] and plays a key role in maintaining protein homeostasis. Full-length HSP27 comprises 205 residues (Fig. 1A) but assembles into large, polydisperse oligomers that have an average mass near 500 kDa [24]. Both the N- and C-terminal regions of HSP27 are involved in oligomerization, and these regions are predominantly intrinsically disordered [25,26,35] (Fig. 1A). Removal of the terminal regions prevents the formation of large oligomers, leaving the isolated ACD that forms stable dimers (Fig. 1B) and can prevent the aggregation of substrate proteins *in vitro* [26,31,34]. Recently, we and others demonstrated that acidic conditions destabilize the HSP27 ACD dimer [26,36] and promote monomer formation [26]. Interestingly, we found that monomerization was coupled to an increase in chaperone activity for both the ACD and full-length protein [26], which suggests that structural rearrangements upon ACD dimer dissociation are related to activity. However, the structural details of the ACD dimer-to-monomer transition are only beginning to be unveiled, largely due to the unstable nature of ACD monomers at elevated concentrations and their low populations under most experimental conditions.

Here, we investigated the structural and dynamical transitions that occur upon dissociation of the HSP27 ACD dimer. Under acidic conditions, the ACD monomer exists in slow exchange alongside the acid-unfolded form, which enables a direct comparison of structural changes between the two states.  $^{13}\text{C}\alpha$  and  $^{13}\text{CO}$  chemical shift perturbations identify large secondary structural changes between the ACD dimer and monomer that are primarily localized to the interfacial region spanning the residues H124–S137. The magnitude of the  $^{13}\text{C}\alpha$  secondary chemical shifts has significantly decreased in this region, suggesting that the ACD monomer is more unfolded. These data are supported by  $^{15}\text{N}$  relaxation rates and diminished  $^1\text{H}$ – $^{15}\text{N}$  residual dipolar couplings (RDCs), which point to large amplitude backbone motions in the interfacial region. Finally, with structural bioinformatics, we assessed the generality of the partial unfolding of ACD monomers. We used previously established methods that can predict the magnitude of structural changes in a monomer upon dissociation

from a complex [37,38], as well as discriminate between monomers that remain structured and those that unfold upon dissociation [39]. Using this approach, we calculated the ratio of per-residue solvent accessible and buried surface areas of all known ACD dimers and compared these ratios to a database of dimers that are known to dissociate into either ordered or disordered monomers. Our results lead to the hypothesis that, upon dissociation from the dimer, sHSP ACD monomers from all kingdoms of life are likely to undergo a similar partial unfolding event as HSP27.

## Results

Here, we have investigated the isolated ACD (cHSP27) comprising residues 84–171 of human HSP27 (Fig. 1B). While cHSP27 primarily exists as a dimer, it can access a monomeric form and unfolded state depending on the concentration and solution conditions (Fig. 1B and C). Our construct includes the C137S mutation, which effectively mimics the reduced form of the wild-type ACD and prevents the formation of an intersubunit disulfide bond [26].

### pH-induced unfolding of cHSP27

Previously, we established that the  $K_d$  for cHSP27 dimerization at pH 7 is ca. 1  $\mu\text{M}$  [26], which renders the population of free monomer below 5–10% at most NMR-tractable concentrations. Like  $\alpha\text{B}$ -crystallin, the monomer-dimer equilibrium of cHSP27 is sensitive to pH [26,33,36]. There are four histidine residues in cHSP27 (Supplementary Fig. 1), with H124 and H131 situated at the dimer interface. Prior work has established that mutation of H124 to Lys, which attempts to mimic H124 protonation, promotes monomerization even at neutral pH [26,36]. However, the H124K variant of cHSP27 is unstable and readily aggregates at NMR concentrations [26], thereby preventing high-resolution insight into the conformation of the monomer.

To find conditions suitable to characterize the cHSP27 monomer, we collected two-dimensional (2D)  $^1\text{H}$ – $^{15}\text{N}$  heteronuclear single quantum coherence (HSQC) spectra of cHSP27 as a function of pH (Fig. 1C, Supplementary Fig. 1). At pH 7 and 250  $\mu\text{M}$ , the sample is predominantly dimeric (Fig. 1C), whereas a mixture of monomer and dimer is evident at pH 6.5 (Supplementary Fig. 1). However, ~15 resonances from residues at the dimer interface and in the  $\beta$ 5-strand become severely broadened at pH 6.5 and are not recovered by lowering the pH to 6 or 5 (Supplementary Fig. 1). Moreover, while the dimer at pH 7 is stable and amenable to NMR experiments at 250  $\mu\text{M}$  and above over a prolonged period of time, the monomer at pH values of 6 and below is both severely exchange-broadened and prone to

aggregation. Thus, we sought to identify conditions that lead to both a stable monomeric sample and high spectral quality.

We obtained high-quality NMR spectra of the monomer at pH 4.2 and a protein concentration of 150  $\mu$ M (Fig. 1C). The 2D  $^1\text{H}$ - $^{15}\text{N}$  HSQC spectrum reveals the transition from predominantly folded dimer at pH 7 to a partially folded monomer at pH 4.2 (Fig. 1C). Increasing the protein concentration to 450  $\mu$ M at pH 4.2 severely decreased the spectral quality (Supplementary Fig. 2), and we thus kept the concentration equal to or below 150  $\mu$ M in all subsequent experiments described here at this pH. Importantly, we previously verified that the  $^{15}\text{N}$

chemical shifts measured directly from the monomer at pH 4.2 closely resemble those of the monomer at pH 7, where the population of the monomer is only  $\sim 1\%$  but was characterized with Carr-Purcell-Meiboom-Gill (CPMG) relaxation dispersion experiments [26,40]. Similar results have also been reported for  $\alpha$ B-crystallin [33], thus establishing that the monomer present at low pH resembles the monomer at physiological conditions.

Two sets of resonances for each residue were evident at pH 4.2 (Fig. 1C), indicating the presence of two structurally distinct conformations that slowly interconvert. We determined that the minor set of resonances originates from the acid-unfolded state,

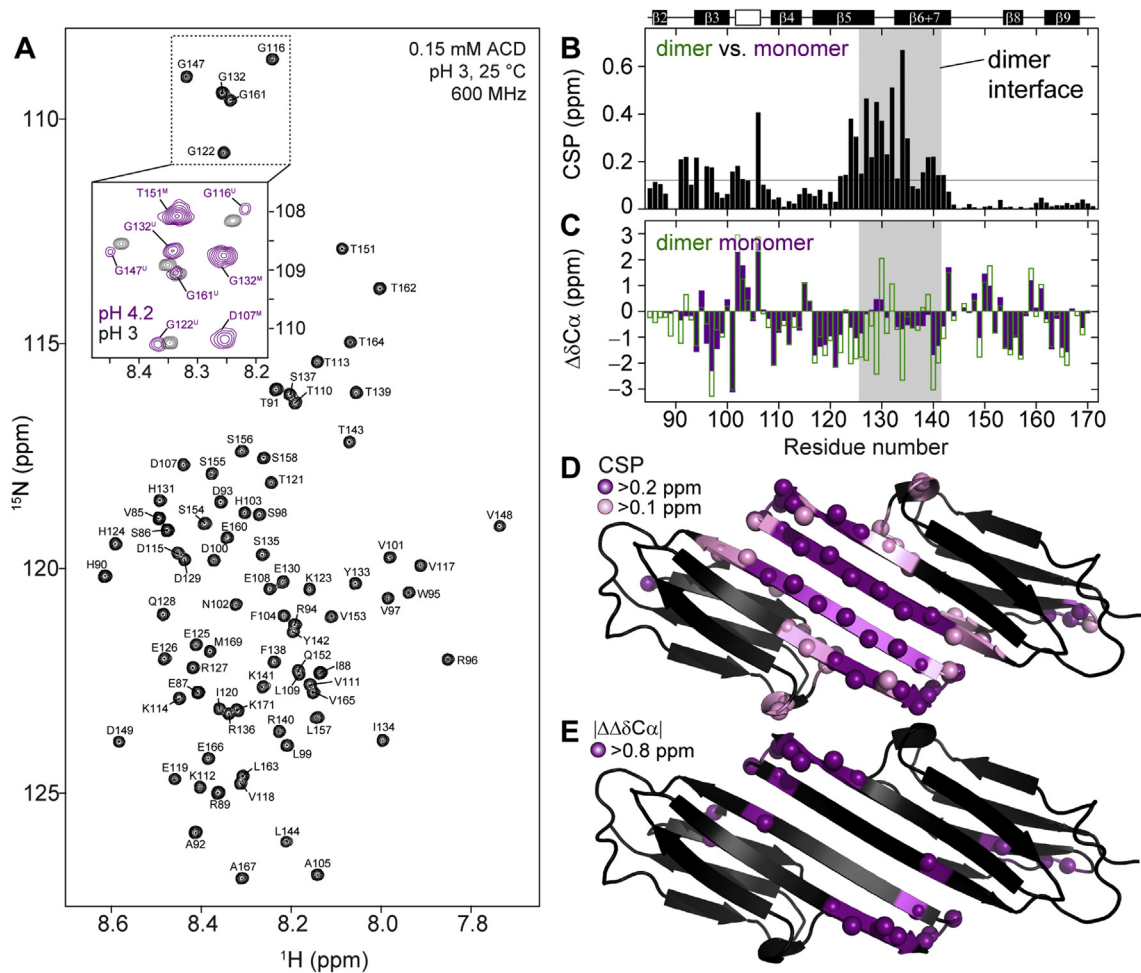


**Fig. 2.** Structural changes upon ACD monomerization and unfolding. (A) Projection of a 3D HNCA spectrum of  $^2\text{H}$ ,  $^{13}\text{C}$ ,  $^{15}\text{N}$ -labeled cHSP27 at pH 3 onto the  $^1\text{H}$  and  $^{15}\text{N}$  dimensions. Resonance assignments are indicated. The inset contains overlaid spectra of cHSP27 at pH 3 (black) and pH 4.2 (purple), with resonance assignments for the unfolded state or monomer at pH 4.2 respectively indicated with a superscript U or M. Combined and weighted  $^{13}\text{CO}$  and  $^{13}\text{C}\alpha$  chemical shift perturbations (CSPs) for (B) the dimer at pH 7 vs. the monomer at pH 4.1. (C) Secondary  $^{13}\text{C}\alpha$  chemical shifts ( $\Delta\delta^{13}\text{C}\alpha$ ) for the monomer (purple) at pH 4.1 and dimer (green) at pH 7. Negative values indicate  $\beta$ -strands. (D) CSPs from panel B mapped onto the structure of the cHSP27 dimer (PDB: 4mjh). The average value of the CSP is 0.11 ppm, with the average plus one standard deviation equal to 0.23 ppm. (E) Residues with large secondary structural changes ( $|\Delta\delta^{13}\text{C}\alpha_{\text{dimer}} - \Delta\delta^{13}\text{C}\alpha_{\text{monomer}}| > 0.8$  ppm) are indicated on the structure of the cHSP27 dimer.

as the relative population of this form increases with decreasing pH (Fig. 1C). At pH 3.7, the populations of the monomeric and unfolded states are roughly equal (Fig. 1C), whereas at pH 3 the unfolded state is the only observable form (Fig. 1C).

### Structural characterization of the cHSP27 monomer

The unfolded state of cHSP27 provides a useful internal standard against which we can compare chemical shifts and other structural parameters to the cHSP27 monomer. We assigned the backbone chemical shifts of unfolded cHSP27 at pH 3 using non-uniformly sampled (NUS) triple-resonance NMR experiments (Fig. 2A). Only small deviations from the predicted, neighbor-corrected random coil chemical shifts [41] were observed (Supplementary Fig. 3), confirming that the protein is fully denatured at pH 3 (Fig. 2B–D). The transition from dimer to monomer occurs in the pH range that encompasses protonation of His side chains ( $pK_a$  values around 6), two of which are at the cHSP27 dimer interface, H124 and H131 (Supplementary Fig. 1). However, the acid-induced unfolding of the cHSP27 monomer is likely caused by the protonation of Asp and Glu sidechains, which have respective  $pK_a$  values around 4.2 and 3.6.

At pH 3, only signals from the unfolded state were observed with no detectable monomer present. We, therefore, raised the pH to 4.1, where approximately 10% of the protein is unfolded, and used the pH 3 assignments to guide assignment of the backbone chemical shifts from the lowly populated unfolded state. We obtained complete  $^1\text{H}^N$ ,  $^{15}\text{N}$ ,  $^{13}\text{C}\alpha$ , and  $^{13}\text{CO}$  chemical shift assignments for both the monomer and the unfolded state at pH 4.1, as well as the dimer at pH 7. These datasets enabled us to calculate structural changes that manifest between all three forms of cHSP27 (Fig. 2B–G), including the dimer-to-monomer, monomer-to-unfolded, and dimer-to-unfolded transitions. To this end, we calculated the combined, weighted  $^{13}\text{C}\alpha$  and  $^{13}\text{CO}$  chemical shift perturbations (CSPs) (Eq. (1), Methods), as these chemical shifts are faithful reporters on secondary structural changes.

First, we assessed structural changes that manifest upon monomerization, *i.e.*, between the monomeric and dimeric forms of cHSP27. The average value of the  $^{13}\text{C}\alpha$  and  $^{13}\text{CO}$  CSPs was 0.11 ppm, and the largest CSPs were observed for residues in the  $\beta_5$  and  $\beta_{6+7}$  strands (Fig. 2B and D): R127, D129, G132, and I134 exhibited CSPs near or above 0.4 ppm, consistent with large structural changes in this region upon monomerization. In addition, small CSPs that are near or above the average value are found in the  $\beta_2$  and  $\beta_3$  strands (Fig. 2B), *e.g.*, 0.11 ppm for S86 and 0.21 ppm for A92. As determined from previous NMR data [26], the  $\beta_2$

strand is likely only transiently formed in the dimer; however, based on the chemical shifts, as well as  $^{15}\text{N}$  relaxation rates (*vide infra*), the  $\beta_2$  strand in the monomer has likely completely unfolded. Finally, there were no significant  $^{13}\text{C}\alpha$  and  $^{13}\text{CO}$  CSPs observed for residues L144–K171 (Fig. 2B), demonstrating that this region in the monomer likely adopts essentially the same structure as that in the dimer.

Next, we compared changes to the secondary structure of monomeric and dimeric cHSP27. We calculated the secondary chemical shifts ( $\Delta\delta$ ) for  $^{13}\text{C}\alpha$  (Fig. 2C), which report on secondary structure. These were determined by calculating the difference between the chemical shift of the monomer or dimer and that of the unfolded state. Negative and positive values of  $\Delta\delta\text{C}\alpha$ , respectively, indicate  $\beta$ -strands and  $\alpha$ -helices, whereas values near zero are indicative of disordered regions. Both the dimer and monomer exhibit very similar and negative  $\Delta\delta\text{C}\alpha$  values in the  $\beta_3$ ,  $\beta_4$ ,  $\beta_8$ , and  $\beta_9$  strands (Fig. 2C), as expected for stable  $\beta$ -strands. By contrast, the region encompassing H124–I134 has significantly less negative  $\Delta\delta\text{C}\alpha$  values in the monomeric form (Fig. 2C), suggestive of decreased  $\beta$ -strand propensity, with  $\Delta\delta\text{C}\alpha$  differences between the dimer and monomer ( $\Delta\Delta\delta\text{C}\alpha$ ) often exceeding +0.8 ppm (Fig. 2C and E). For example, the average  $\Delta\delta\text{C}\alpha$  values for the C-terminal portion of  $\beta_5$  (H124–Q128) and N-terminal portion of  $\beta_{6+7}$  have, respectively, decreased from  $-1.62$  and  $-1$  ppm in the dimer to  $-0.51$  and  $-0.4$  ppm in the monomer (Table 1). These data indicate that the  $\beta_3$ ,  $\beta_4$ ,  $\beta_8$ , and  $\beta_9$  strands are similar between the monomer and dimer, but the C-terminal portion of  $\beta_5$ ,  $L_{5,6+7}$ , and the N-terminal portion of  $\beta_{6+7}$  are more disordered in the monomer.

### Backbone dynamics of the cHSP27 monomer

Having established that the cHSP27 monomer exists in slow exchange with a small population of an acid-unfolded state at low pH, we characterized both conformations simultaneously using NMR experiments that are sensitive to backbone motions. We recorded TROSY-based  $^{15}\text{N}$  longitudinal (Fig. 3A and B) and transverse (Fig. 3C and D) relaxation rates ( $R_1$  and  $R_2$ ) and heteronuclear nuclear Overhauser effects ( $^{15}\text{N}\{^1\text{H}\}$  NOEs) (Fig. 3E) in both the cHSP27 dimer and monomer to quantify the amplitude of backbone dynamics. These spin relaxation parameters are effective probes of molecular motions on the pico-nanosecond timescale, as well as the global rotational correlation time of a molecule. The  $^{15}\text{N}$   $R_2/R_1$  ratios yielded an isotropic rotational correlation time ( $\tau_c$ ) for the monomer (Eq. (2), Methods) of  $6.0 \pm 0.8$  ns (Fig. 3F), which for a spherical particle corresponds to a hydrodynamic radius (Eq. (3), Methods) of  $17 \pm 2$  Å at 15 °C. These values are consistent with a 9.8 kDa protein, where

**Table 1.** Combined, weighted  $^{13}\text{C}\alpha$  and  $^{13}\text{CO}$  chemical shift perturbations for the cHSP27 monomer and dimer upon unfolding. For each  $\beta$ -strand, the associated residues and average chemical shift perturbation are listed. The  $\langle \rangle$  brackets indicate the average value over the indicated region, and the superscript  $^{\text{N}}$  and  $^{\text{C}}$  respectively refer to the N- and C-terminal portions of the indicated strand. M, D, and U stand for the monomeric, dimeric, and unfolded forms of cHSP27, respectively. The  $\Delta^{\Delta\delta}$  symbol refers to the difference between the  $\Delta\delta\text{C}\alpha$  values (dimer–monomer).

Region	Residues	$\langle \Delta\delta\text{C}\alpha^{\text{M}} \rangle$ (ppm)	$\langle \Delta\delta\text{C}\alpha^{\text{D}} \rangle$ (ppm)	$\Delta^{\Delta\delta}$ (ppm)
$\beta 3$	R94-L99	-1.09	-1.11	-0.02
$\beta 4$	L109-K114	-0.91	-0.99	-0.08
$\beta 5$	V117-Q128	-0.91	-1.47	-0.56
$\beta 5^{\text{N}}$	V117-K123	-1.19	-1.36	-0.17
$\beta 5^{\text{C}}$	H124-Q128	-0.51	-1.62	-1.11
$\text{L}_{5,6+7}$	D129-G132	-0.08	-0.74	-0.66
$\beta 6+7$	Y133-T143	-0.50	-0.79	-0.29
$\beta 6+7^{\text{N}}$	Y133-S137	-0.60	-1.00	-0.40
$\beta 6+7^{\text{C}}$	F138-T143	-0.42	-0.63	-0.21
$\beta 8$	S154-L157	-1.40	-1.48	-0.08
$\beta 9$	T162-E166	-1.00	-1.16	-0.16

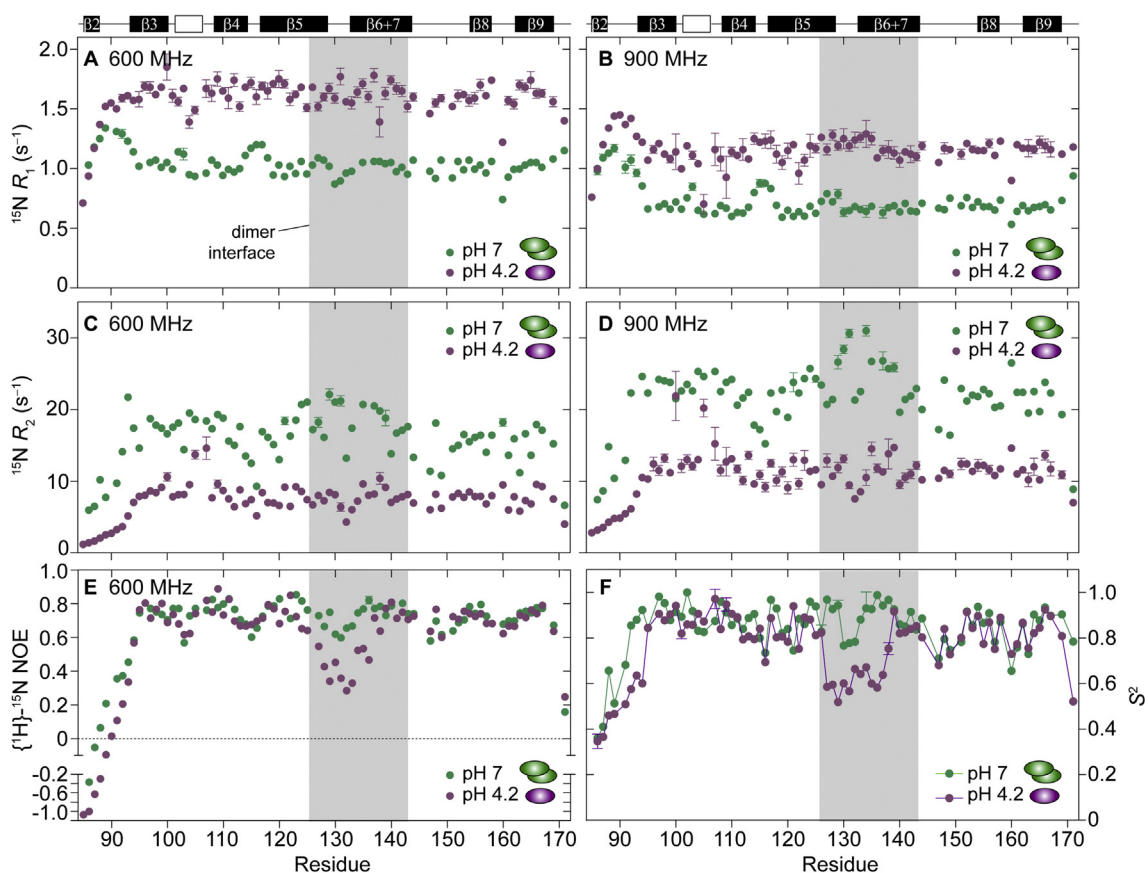


**Fig. 3.** Backbone dynamics of the cHSP27 dimer and monomer.  $^{15}\text{N}$  spin relaxation data recorded on the cHSP27 dimer at pH 7 (green) and cHSP27 monomer at pH 4.2 (purple).  $^{15}\text{N}$   $R_1$  rates recorded at a static magnetic field strength of (A) 600 and (B) 900 MHz,  $^{15}\text{N}$   $R_{1\rho}$  rates that were converted to  $R_2$  rates at (C) 600 and (D) 900 MHz, and  $^{15}\text{N}\{^1\text{H}\}$  NOEs measured at 600 MHz (E). Lipari-Szabo model-free analysis of the  $^{15}\text{N}$  relaxation data from the dimer at pH 7 (green) and the monomer at pH 4.2 (purple). The squared generalized order parameters  $S^2$  are reported here (F).

empirical equations predict a hydrodynamic radius of 17.3 Å for a globular protein of this size [42]. In comparison, our  $^{15}\text{N}$  spin relaxation experiments on the cHSP27 dimer at pH 7 yield a  $\tau_c$  value of  $12.5 \pm$

1.6 ns (Fig. 3E), which is consistent with a  $2 \times 9.8$  kDa protein at 15 °C. Assuming a spherical particle, the calculated hydration radius of  $21.8 \pm 2.8$  Å agrees closely with the 21.1 Å radius expected

from empirical equations [42]. Our  $^{15}\text{N}$  spin relaxation measurements unambiguously establish that the cHSP27 sample at low pH is monomeric.

The  $^{15}\text{N}$  relaxation data offer additional insight into the backbone motions in the cHSP27 monomer. The N-terminal residues V85-D93 exhibit strongly reduced  $R_2$  rates and  $^{15}\text{N}\{^1\text{H}\}$  NOEs that are indicative of high mobility (Fig. 3C–E), demonstrating that the  $\beta 2$  strand is at most only transiently present for a small fraction of the time. Conversely, while the  $^{15}\text{N}$  relaxation rates in the dimer also indicate that the  $\beta 2$  strand is not stably formed, as this region has  $^{15}\text{N}\{^1\text{H}\}$  NOE values below 0.1 and  $R_2$  rates in the 7–10  $\text{s}^{-1}$  range at 600 MHz (Fig. 3C and E), it clearly also is transiently ordered as also evidenced by its secondary chemical shifts and RDCs (vide infra). Thus, while the low pH of the buffer used to study the monomeric sample may have impacted the conformational dynamics of the  $\beta 2$  strand, our finding that  $\beta 2$  is only transiently present in the dimer indicates that it is only marginally stable. These results agree with previous NMR data on ACD of the similar protein  $\alpha\text{B}$ -crystallin, in which it was found that the  $\beta 2$  strand was not stably formed in solution [43].

Additional differences between the backbone dynamics of the monomer and dimer are evident from our  $^{15}\text{N}\{^1\text{H}\}$  and  $R_2$  data, which indicate that residues R127–R136 in the monomer become more mobile on the picosecond timescale. This is evidenced by  $^{15}\text{N}\{^1\text{H}\}$  NOE values that are all lower than 0.6 at 600 MHz (Fig. 3E) and a local minimum in the  $R_2$  rates at G132 (Fig. 3C and D). Overall, the  $^{15}\text{N}$  relaxation data of the monomer are consistent with our chemical shift analysis above (Fig. 2) and indicate that the interfacial region partially unfolds and becomes more mobile upon dissociation. To gain additional insight into the backbone dynamics of the cHSP27 monomer, we fit our  $^{15}\text{N}$  relaxation to Lipari–Szabo models [44] that describe the amplitude and timescale of internal motions. The generalized squared order parameter ( $S^2$ ) respectively varies from 0 to 1 for a fully disordered and a completely rigid bond vector, and an internal correlation time ( $\tau_e$ ) captures rapid motions on the ps timescale. We fit the  $^{15}\text{N}$  relaxation data from the monomer to Lipari–Szabo models using a local  $\tau_c$  parameter. Across the rest of the monomer, excluding the dynamic residues at the interface and those at the N-terminus, we find that the average  $\tau_c$  value obtained from our Lipari–Szabo modeling is  $5.89 \pm 0.80$  ns (Supplementary Fig. 4), which closely agrees with the global  $\tau_c$  that we obtained from analysis of the trimmed  $^{15}\text{N}$   $R_2/R_1$  ratios ( $6.0 \pm 0.8$  ns) (Methods).

When we compare the  $S^2$  values of the monomer to the dimer, we find that the loop between  $\beta 2/\beta 3$  and the interfacial region spanning residues R127–F138 show the largest differences in  $S^2$  values. Indeed,

the dimer shows some flexibility in the loop between the  $\beta 5/\beta 6+7$  strands, as evidenced by locally diminished  $S^2$  values for E130–G132 (ca. 0.75); however, the monomer exhibits considerably more flexibility in this region and the adjacent residues, indicating that the C-terminal region of  $\beta 5$  and the N-terminal region of  $\beta 6+7$  are not stably formed. We note that the Lipari–Szabo analysis requires a clear separation in the timescales of motion, and therefore our fitted parameters for the monomer may be prone to error. Nonetheless, the raw relaxation data indicate that the interfacial region exhibits larger amplitude backbone motions with rapid timescale motions.

### Residual dipolar couplings provide additional structural insight

In order to better characterize the structural changes that occur upon cHSP27 monomerization, we recorded  $^1\text{H}$ – $^{15}\text{N}$  residual dipolar couplings (RDCs), which report on N–H bond vector orientations within a common reference frame [45]. We partially aligned samples of the cHSP27 dimer or monomer in solutions of PEG-hexanol (Methods) and measured N–H RDCs ( $^1D_{\text{NH}}$ ) using standard methods [46] (Fig. 4). To accurately determine the alignment tensor of the dimer (Table 2), we first fit a subset of the measured RDCs to the crystal structure of the cHSP27 dimer (PDB: 4mjh). Since the crystal structure is only available at a resolution of 2.6 Å, and thus contains considerable structural noise [47], we chose residues in well-defined regions of secondary structure and without evidence of exchange, measured previously [26], in order to better define the alignment tensor. Thus, we fit  $2 \times 19$  couplings to 38 N–H bond vectors in the cHSP27 crystal structure of the dimer to obtain the alignment tensor (Table 2). For the RDCs that were not used to determine the alignment tensor, the correlation between measured and predicted  $^1D_{\text{NH}}$  values is reasonable, with deviations in some residues (Fig. 4B) indicating different orientations of these N–H bond vectors in solution compared to the crystalline state. For  $n = 45$  residues in secondary structural elements, the Q factor (Eq. 4, Methods) [48], reflecting the agreement between the measured RDCs and the predictions based on the crystal structure, is 37% (Supplementary Fig. 5) and matches the expectations for a 2.6-Å structure [49]. The Q factor increases to 49% when all residues are included in the analysis (Supplementary Fig. 5), which is to be expected due to the poorly defined atomic positions of N–H bond vectors in loop regions and the known flexibility of the  $\beta 2$ -strand [50].

For the monomer, we fit  $^1D_{\text{NH}}$  values from the same set of residues as above to obtain the alignment tensor (Table 2). These 19 RDCs were

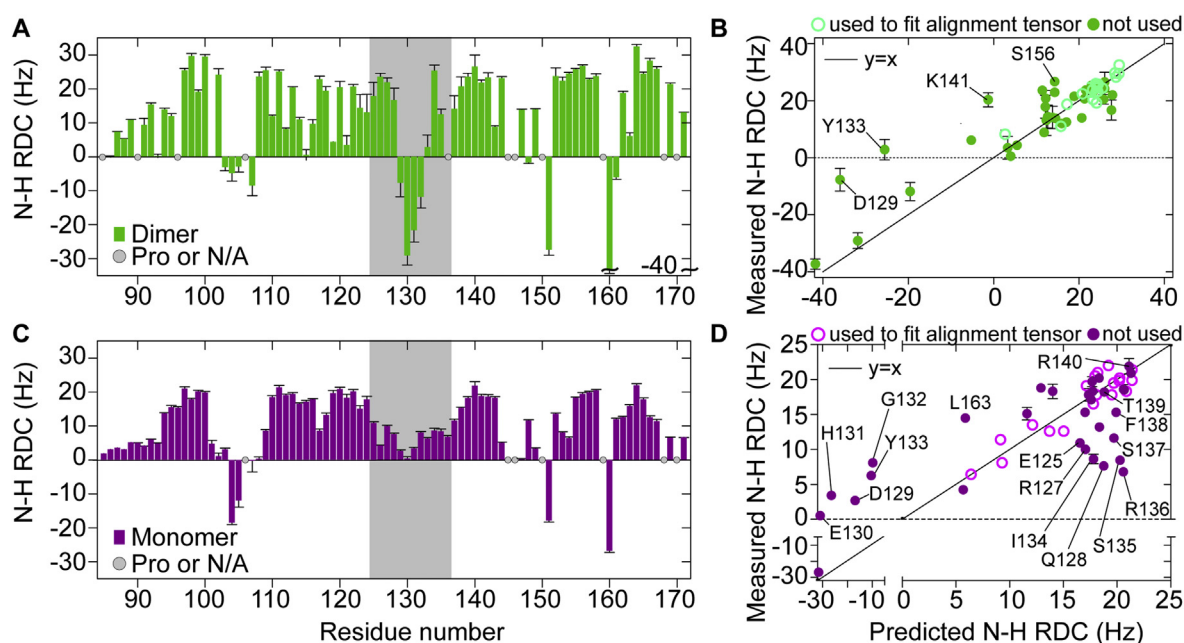


**Fig. 4.** Structural analysis of the cHSP27 dimer and monomer with RDCs.  $^1\text{H}$ – $^{15}\text{N}$  residual dipolar couplings (RDCs) for the cHSP27 dimer (A) or monomer (C) aligned in the presence of 4.3% (v/v) PEG-hexanol. The grey box indicates the region with large  $^{13}\text{C}\alpha$  and  $^{13}\text{CO}$  CSPs. RDCs from residues in well-defined regions of secondary structure were used to determine the alignment tensor that was then used to predict RDCs based on the crystal structure of the dimer (B) or one chain from the dimer (D). Outliers are indicated on the correlation plot. For the dimer, the outliers likely originate from structural noise in the 2.6-Å crystal structure. For the monomer, outliers largely cluster to the  $\beta 5$ ,  $L_{5,6+7}$ , and  $\beta 6+7$  regions, indicative of a structural rearrangement relative to the crystal structure.

**Table 2. Alignment tensors of the cHSP27 dimer and monomer in 4.3% PEG-hexanol.** The measured values of  $^1D_{\text{NH}}$  for either the cHSP27 dimer or monomer were fit to the crystal structure (PDB: 4mjh) using SVD to determine the magnitude ( $D_a$ ) and rhombicity ( $R$ ) of the alignment tensor, as well the Euler angles ( $\alpha$ ,  $\beta$ ,  $\gamma$ ) that describe its orientation relative to the molecular frame. The magnitude reported here ( $D_a^{\text{NH}}$ ) has been normalized to the N–H couplings. The number of couplings used to determine the alignment tensor are indicated in the final column, with 19 x 2 indicating the symmetric nature of the cHSP27 dimer.

Sample	$D_a^{\text{NH}}$ (Hz)	$R$	$\alpha$ (°)	$\beta$ (°)	$\gamma$ (°)	# of couplings
Dimer, pH 7	–26.2	0.085	–7.0	–2.3	85.7	19 x 2
Monomer, pH 4.2	–15.9	0.23	15.1	5.9	110.8	19

fit to 19 N–H bond vectors in chain A of the cHSP27 crystal structure (PDB: 4mjh), henceforth referred to as the “rigid body monomer.” For many residues, including 14 not used for the fitting, the back-calculated  $^1D_{\text{NH}}$  values closely matched the measured values (Fig. 4D), yielding a Q factor of 23% for  $n = 33$  residues in regions of secondary structure (Supplementary Fig. 5). However, the region spanning E125–S137 showed substantial deviations between the predicted and measured values (Fig. 4D), with lower values of  $^1D_{\text{NH}}$  than expected from the rigid body monomer structure. This region, encompassing the C-terminal portion of  $\beta 5$ ,  $L_{5,6+7}$ , and the N-terminal portion of  $\beta 6+7$ , therefore samples different conformations in solution relative to the rigid body monomer. Interestingly, the RDCs

from residues just up or downstream of this region, namely E119–H124 in the N-terminal portion of  $\beta 5$  and F138–T143 in the C-terminus of  $\beta 6+7$ , actually agree well with the back-calculated values and have respective RMSD values (predicted vs. measured) of 2.5 and 3.2 Hz. These results indicate that the respective conformations of the N- and C-terminal portions of  $\beta 5$  and  $\beta 6+7$  in solution resemble that of the rigid body monomer, whereas the intervening region has become more disordered. Combined with the decreased values of  $\Delta\delta\text{C}\alpha$  (Fig. 2C) and diminished  $^{15}\text{N}\{^1\text{H}\}$  NOEs and  $S^2$  values (Fig. 3E and F) in the interfacial region, our RDCs measurements point to a more flexible conformation with the lower than expected values of  $^1D_{\text{NH}}$  caused by dynamical averaging.

## Disordered monomers in other sHSPs

In light of our findings above, and given the conserved structural features of ACDs, we wondered if the dissociation-induced unfolding of ACD dimer interfaces may be a general feature of this class of chaperone. Previous structural bioinformatics studies have demonstrated that the solvent-accessible surface area (SASA) of a protein relative to that expected from its molecular weight can be used to predict the magnitude of structural rearrangements that occur upon complex formation or dissociation [37,38]. In addition, per-residue calculations of the SASA and buried surface area (BSA) for subunits within a complex can discriminate between oligomers that dissociate into ordered or disordered monomers [39]. We used these metrics to assess whether ACD dimers from other sHSPs would also partially unfold upon dissociation.

First, we computed the ratio of per-residue SASA and per-residue BSA, henceforth referred to as the disorder index, for dimers that are known to dissociate into disordered monomers. These dimers were extracted from the Mutual Folding Induced Binding (MFIB) database [51]. The disorder indices of these dimers sample a distribution centered at 2.2, with the vast majority falling between 1.5 and 3 (Fig. 5A). We next calculated the same metrics for dimers that are known to dissociate into structured monomers. The distribution of disorder indices for

these dimers is shifted to significantly lower values, with the center near 1.2 (Fig. 5A).

Having established that the disorder index is a valuable metric to discriminate dimers that dissociate into ordered or disordered monomers, we then calculated the disorder indices for 39 structures of sHSPs or their ACDs (Fig. 5A). Remarkably, the distribution of disorder indices for ACD dimers is centered around 1.8 (Fig. 5A), including human HSP27 (1.69), human  $\alpha$ B-crystallin (2.03), *C. elegans* Sip1 (1.89), and archaeal Hsp16.5 (1.74), indicating that the monomers likely undergo at least partial unfolding. The range of disorder indices for ACDs spans 1.4–2.2, which slightly overlaps with some of the dimers known to dissociate into structured monomers; however, the overlap between disordered monomers and the sHSPs is significantly larger (Fig. 5A). Importantly, the disorder index is not significantly changed when considering other structural regions outside of the ACD: e.g., for the structure of the 24-mer of Hsp16.5 from *M. janaschii*, the disorder index for the full-length protein is 1.76 compared to 1.75 when analyzing only the ACD. Similarly, for Hsp16.9 that has been crystallized as a 12-mer, the disorder index for the full-length protein is 2.2 compared to 2.0 for the ACD only. These values were similar to the disorder indices calculated for the Arc repressor (2.01), a non-covalent dimer that adopts a disordered molten globule conformation upon

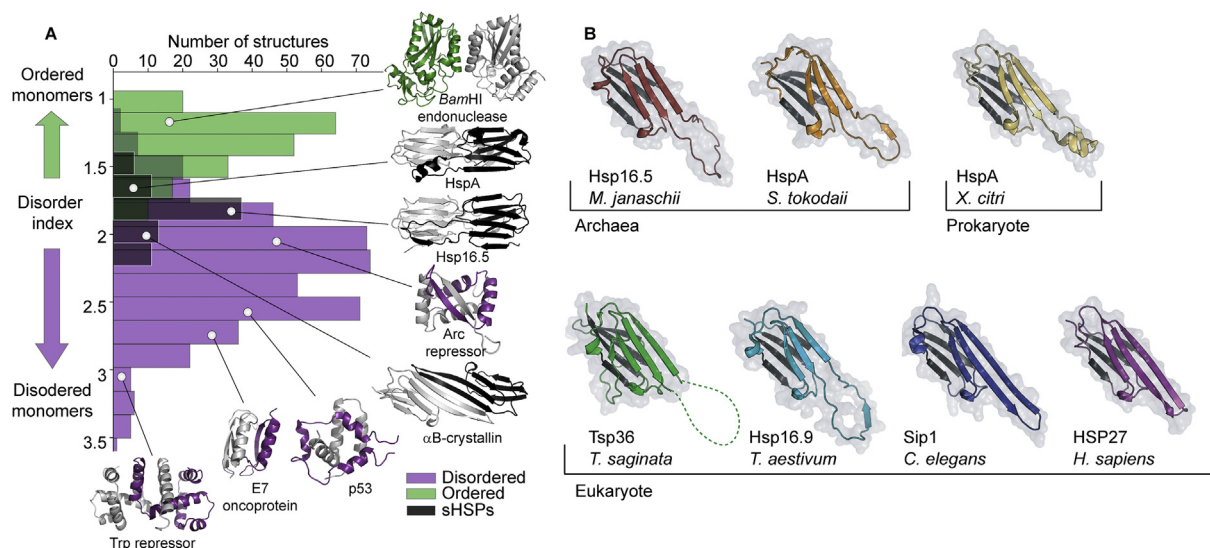


**Fig. 5.** Partial unfolding upon ACD dimer dissociation is likely a general property. (A) Disorder indices, calculated as the ratio of per-residue SASA to per-residue BSA for each protein in a complex, discriminate between dimers that dissociate into ordered (green) or disordered (purple) monomers. sHSP ACDs (black) largely overlap with the disordered monomers, suggesting that ACD monomers undergo at least partial unfolding upon dissociation. The structures depict examples from the various groups: BamHI endonuclease (PDB: 1BAM; 1.18), HspA (PDB: 3GLA; 1.67), Hsp16.5 (PDB: 1SHS; 1.75), Arc repressor (PDB: 1ARQ; 2.01),  $\alpha$ B-crystallin (PDB: 2KLR; 2.03), p53 TAD bound to NCBD (PDB: 2L14; 2.52), HPV E7 CR3 domain (PDB: 2B9D; 2.87), and the DNA-binding domain of Trp repressor (PDB:3WRP; 3.00). (B) Structures of ACD dimers from all kingdoms of life. Only one chain from each dimer is shown here for clarity. The protein and organism names are listed under each structure.

dissociation [52]; the transactivation domain of p53 in complex with the NCBD of CBP (2.52) [53]; and HdeA (1.90), an *E. coli* molecular chaperone that exists as an inactive dimer, but dissociates into disordered monomers that are highly active [54]. Therefore, this analysis suggests that the partial unfolding of sHSP ACD dimers upon dissociation may be a general property of sHSPs.

## Discussion

Here, we have studied the structure and dynamics of the HSP27 ACD monomer in solution by means of NMR spectroscopy. Given that most ACD dimers reportedly have dissociation constants in the low  $\mu\text{M}$  range (e.g., 1–5  $\mu\text{M}$ ), there is likely a significant monomeric fraction inside cells, where, notwithstanding molecular crowding conditions, the protein concentration is expected to be significantly below the dimerization  $K_d$  [55]. Moreover, because odd-numbered oligomers are routinely detected by *in vitro* native mass spectrometry experiments, this also means that monomeric ACDs exist within full-length oligomeric sHSPs [18,21,24,26]. However, while numerous studies have interrogated the structures and biophysical properties of ACD dimers, much less focus has been placed on the monomeric state of this domain [26,27]. To our knowledge, our study represents the most comprehensive characterization of an ACD monomer to-date and outlines potentially general protocols and methods that can be used to investigate monomeric ACDs from other sHSPs. The conditional disorder that is encoded within ACD dimers adds to the growing significance of the role of intrinsic disorder within sHSPs and functional disorder within molecular chaperones [56,57]. In particular, conditional disorder and structural plasticity seem widespread within the family of ATP-independent chaperones [58].

Our NMR data highlight the structural plasticity that exists within the dimer interface of HSP27, encompassing the region H124–S137 that has partially unfolded upon monomerization. While we have characterized the monomer here in a low pH buffer, previous NMR measurements indicate that the structure of the monomer at pH 7 is similar to that at low pH [26]. However, since the population of the monomer at pH 7 is only ~1%, we lowered the pH to increase the abundance, and hence allow direct observation of the partially unfolded monomeric state. Collectively, the  $^{13}\text{C}\alpha$  and  $^{13}\text{CO}$  CSPs,  $^{13}\text{C}\alpha$  secondary chemical shifts, N–H RDCs, and  $^{15}\text{N}$  relaxation rates point to a more disordered region in the monomer. These data conclusively establish that the dimer interface becomes highly dynamic and flexible in the monomeric state. Along with the intrinsically disordered N- and C-terminal regions, the partially unfolded dimer interface contributes to

making HSP27 a conditionally disordered [56] molecular chaperone. In large HSP27 oligomers, we note that the N-terminal region, while disordered, likely retains some structure because this region is undetectable in solution-state NMR spectra of the wild-type protein, whereas the C-terminal region is always observed [35]. By contrast, the N-terminal region can be readily detected in NMR spectra of the full-length dimeric protein [25] under conditions where biochemical studies have established that the N-terminus becomes more exposed to solvent [59]. Therefore, both the N-terminal region and the dimer interface become more disordered under conditions that promote oligomer dissociation, rendering HSP27 a conditionally disordered chaperone. Importantly, the interfacial region that we found partially unfolds is primarily comprised of polar and charged residues, which account for 13 of the 14 residues, of which six are charged. This site could potentially be used by HSP27 to interact with unfolded substrates in an electrostatic manner, which would allow for interactions over a longer range. Such electrostatic interactions could be vital for the early-stage role of sHSPs in recognizing the initial steps of protein misfolding. A long-range, electrostatic-based substrate recognition mechanism has been established for the ATP-independent molecular chaperone Spy [60]. It will be interesting to establish whether HSP27 or related sHSPs indeed use their partially unfolded interfacial region to bind substrates and if the chaperone activity or substrate interaction is impacted by the addition of increasing concentrations of salt. A disordered, 8-residue peptide from the  $\beta_{6+7}$  strand of the chaperone  $\alpha\text{B}$ -crystallin is known to prevent the aggregation of substrate proteins [61], pointing to a potential functional role for the disordered interfacial region of the monomer.

Our  $^{15}\text{N}$  relaxation measurements point to nanosecond timescale motions in functionally important regions of HSP27. This is evident by the locally enhanced  $R_1$  rates for  $L_{2,3}$  and  $L_{4,5}$  in the dimer. The same regions of the monomer do not show such local maxima, suggesting that the timescale of backbone motions in  $L_{2,3}$  and  $L_{4,5}$  approaches that of tumbling. The key residues S78 and S82, whose phosphorylation impact HSP27 oligomeric assembly and function [24], lie just N-terminal of  $L_{2,3}$ . Since  $L_{2,3}$  is known to transiently interact with other regions of HSP27, such as  $L_{3,4}$  [50], the nanosecond motions in  $L_{2,3}$  may impact on the conformation of the  $\beta_2$  strand and the overall accessibility of S78 and S82. Similarly, the  $R_1$  rates point to nanosecond motions at the dimer interface at E126–D129. In the crystal structure, the residues E126–D129 residues form inter-protomer salt bridges between E126 and K141' and D129 and R140' (where' refers to the other protomer) that stabilize the dimer interface. In solution, however, the residues E126–D129 in the

dimer appear mobile on the nanosecond timescale. There are multiple disease-causing mutations that fall in this region of HSP27, including R127W and Q128R, and it is tempting to speculate that perturbations to the local backbone motions may play a role in dysregulation of the protein in disease.

ACD dimers share structural features, and therefore, the mechanism of partial unfolding upon monomerization may be similar in sHSPs from other organisms. We assessed this more generally through structural bioinformatics, which led to our prediction that ACD dimers indeed have a high tendency to unfold upon dissociation. Further experiments are required to test this hypothesis. However, since sHSPs and ACDs are found in all kingdoms of life, the structural plasticity that is encoded within the ACD, such that the interfacial region appears only to be structured when contacting another subunit is present, could be widespread and conserved across evolution. While the primary sequences of disordered regions are typically not positionally conserved [62], the interfacial region of sHSPs is conserved among orthologues and suggests that the additional constraint of being structured in ACD dimers establishes positional sequence conservation. Along these lines, it is interesting to note that the amino acid compositions of ACDs lie at the boundary of those for structured and disordered proteins [15], suggesting that the physiochemical properties of these amphipathic domains are useful for the chaperone mechanism of sHSPs.

However, not all sHSP monomers are known to exhibit an increased ability to prevent substrate aggregation, as has recently been established for two plant sHSPs that were disulfide cross-linked across their dimer interface yet remained more active than the reduced forms [63]. The polydisperse nature of human sHSPs renders them particularly challenging to investigate at the biochemical and atomic levels, and the monomer represents but one oligomeric form of sHSPs. The oligomeric states of sHSPs involve coupled equilibria that shift not just with concentration but also environmental factors, including pH and post-translational modifications. As such, multiple oligomeric forms are likely relevant to function and regulation thereof. Under acidosis, the lower pH values are likely to promote monomer formation, but multiple modes of interaction between disparate regions of sHSPs, e.g., NTD-ACD, ACD-ACD, ACD-CTR, contribute to a complicated oligomerization mechanism that also allows larger oligomers to form under such conditions [36]. Our investigation of the structural and dynamical properties of the HSP27 ACD monomer offers a step forward toward understanding one of the more elusive conformations of sHSPs. Future work toward establishing the specific mechanisms of sHSP

chaperone activity and substrate binding will prove essential in elucidating the role of partial ACD unfolding.

## Methods

### Protein expression and purification

The cHSP27 construct used here includes residues G84–K171 of human HSP27 (*HSPB1*) and the C137S mutation to prevent disulfide bond formation. As described previously [26], the C137S mutation does not perturb the structure or dynamics of the cHSP27 dimer and effectively mimics the reduced state of the protein. The expression plasmid contains an N-terminal hexahistidine tag followed by a tobacco etch virus (TEV) protease cleavage site. The Gly overhang following TEV protease cleavage corresponds to G84 in the HSP27 amino acid sequence.

cHSP27 was expressed as described previously [26]. Briefly, BL21(DE3) cells were transformed with the expression plasmid (Kanamycin resistant) and grown in the presence of 30 µg/mL Kanamycin. Following overnight growth at 37 °C with shaking, the cells were pelleted and resuspended in M9 Minimal Medium containing the relevant isotopes for NMR studies. For <sup>2</sup>H, <sup>13</sup>C, <sup>15</sup>N-labeled cHSP27 samples, the medium was prepared in D<sub>2</sub>O (Cambridge Isotope Laboratories, Boston, MA) and contained <sup>15</sup>N ammonium chloride (Sigma-Aldrich) and <sup>2</sup>H/<sup>13</sup>C D-glucose (Cambridge Isotope Laboratories) as the sources of deuterium, nitrogen, and carbon. The medium was supplemented with 1 g/L of <sup>2</sup>H, <sup>13</sup>C, <sup>15</sup>N-labeled ISOGRO (Sigma-Aldrich). The cells grew at 37 °C with shaking until reaching an OD of ca. 1, after which 1 mM IPTG was added to the culture, and protein was expressed at 37 °C for 4 h. Cells were then pelleted and stored at –80 °C until use. Protein purification followed protocols outlined previously, including purification over a Ni<sup>2+</sup> resin column, cleavage of the His-tag by His-tagged TEV protease, separation by reverse-Ni<sup>2+</sup> affinity purification, and gel filtration chromatography [26].

### Disorder prediction

The amino acid sequence of HSP27, UniProt ID P04792, was used as input for the software DISOPRED3 [64]. Default parameters were used for each software to predict the disordered regions of HSP27. Changing C137 to Ser, as in the C137S mutation used for our NMR studies, only slightly increases the predicted levels of disorder around this residue. The values for wild-type HSP27 are reported in Fig. 1.

### NMR spectroscopy

For NMR spectra of the dimer, cHSP27 samples were dissolved in pH 7 buffer containing 30 mM sodium phosphate and 2 mM EDTA, with 6% D<sub>2</sub>O added for the lock. The pH of this buffer was lowered to 4.2, 4.1, 3.7, and 3.0 to shift the dimer-monomer and monomer-unfolded

equilibria to the monomer and unfolded states. Samples of cHSP27 monomer were generally kept to 150  $\mu\text{M}$  or below to minimize the adverse effects observed at higher concentrations that arise from inter-molecular contacts (Supplementary Fig. 2), which eventually lead to aggregation of the monomer [26]. NMR spectra were recorded on 600 or 900 MHz Bruker Avance-III spectrometers equipped with z-axis pulsed-field gradient cryogenic probes. All NMR spectra were processed with NMRPipe [65] and visualized with NMRFAM-Sparky [66]. For experiments that required quantitation of intensities, peak shapes were fit with the program FuDA [67].

### Backbone resonance assignments

Backbone resonance assignments are available for the oxidized form of the cHSP27 dimer [26,32] (BMRB Entries 27046 and 25645). We previously assigned the backbone resonances of the C137S dimer and monomer [26], but extended our assignments here to study of the unfolded state in equilibrium with the monomer. The monomer samples used for NMR analyses were perdeuterated to enhance spectral resolution and exploit the more favorable relaxation properties. Therefore, we recollected assignment spectra on the cHSP27 dimer to enable direct comparison of the chemical shifts. This also avoids potential artifacts introduced by large one-bond deuterium isotope shifts [68] and the dependence of deuterium isotope shifts on the secondary structure [69]. 3D HNCA and HNC0 experiments were recorded at 600 MHz on  $^2\text{H}$ ,  $^{13}\text{C}$ ,  $^{15}\text{N}$ -labeled samples of cHSP27 dimer (pH 7), cHSP27 monomer (pH 4.1), and acid-unfolded cHSP27 (pH 3). The triple resonance spectra were recorded with non-uniform sampling in the indirect dimensions with a sparsity of 10% prior to the extension of the time domains. The full spectra were reconstructed with SMILE [70]. For the dimer and monomer, the HNC0 (HNCA) spectra were acquired with acquisition times of 49.3 ms (49.3 ms), 33.1 ms (11.0 ms), and 127.8 ms (122.9 ms) for the  $t_1$  ( $^{15}\text{N}$ ),  $t_2$  ( $^{13}\text{CO}$  or  $^{13}\text{C}\alpha$ ), and  $t_3$  ( $^1\text{H}$ ) dimensions, respectively. Similar acquisition times were used for the unfolded state, except for a longer maximum acquisition time in the  $t_1$  ( $^{15}\text{N}$ ) dimension. In total, we obtained complete backbone assignments for the cHSP27 monomer, excluding the extreme N-terminus G84 and P145, which is adjacent to P146, and therefore, invisible in these HN-based 3D experiments. The complete list of assignments includes 87  $^{13}\text{C}\alpha$ , 80  $^{13}\text{CO}$ , 80  $^{15}\text{N}$ , and 80  $^1\text{H}^{\text{N}}$  chemical shifts and has been deposited to the BMRB (Entry 28034).

The combined, weighted  $^{13}\text{C}\alpha$  and  $^{13}\text{CO}$  CSPs were determined using the following equation:

$$^{13}\text{C}\alpha + ^{13}\text{CO CSP} = \sqrt{\frac{1}{2} \left( \frac{\Delta\text{C}\alpha^2}{12} + \frac{\Delta\text{C}\text{O}^2}{12} \right)} \quad (1)$$

### Backbone dynamics

By using previously described pulse sequences [71], we recorded heteronuclear TROSY-based  $^{15}\text{N}$  longitudinal ( $R_1$ ), transverse ( $R_{1\rho}$ ), and heteronuclear  $^{15}\text{N}\{^1\text{H}\}$  NOE

relaxation data on the cHSP27 dimer, monomer, and unfolded state.  $^{15}\text{N}$   $R_1$  and  $R_{1\rho}$  data were collected on spectrometers operating at  $^1\text{H}$  frequencies of 600 and 900 MHz; however,  $^{15}\text{N}\{^1\text{H}\}$  data were only recorded at 600 MHz. The samples were uniformly labeled with  $^2\text{H}$ ,  $^{13}\text{C}$ , and  $^{15}\text{N}$  and prepared at protein concentrations of 1 mM in 30 mM sodium phosphate and 2 mM EDTA, with 6%  $\text{D}_2\text{O}$  added for the lock, at pH 7 buffer (dimer) or 0.1 mM in the same buffer at pH 4.2 (monomer plus unfolded). The temperature was set to 15  $^\circ\text{C}$  for these experiments. The relaxation experiments were acquired with acquisition times of 46.8 ms ( $t_1$ ,  $^{15}\text{N}$ ) and 81.1 ms ( $t_2$ ,  $^1\text{H}$ ) with 7 delay times ranging from 0.31 to 2.33 s (dimer,  $R_1$ ) and 10–80 ms (dimer,  $R_{1\rho}$ ) to 0.23–1.55 s (monomer,  $R_1$ ) to 10–200 ms (monomer,  $R_{1\rho}$ ). Errors in the derived relaxation rates were obtained from fitting.  $R_{1\rho}$  measurements were performed using a spin-lock field strength of 1 kHz, and the reported  $R_2$  values were derived from the known relation and corrected for the off-resonance titled field using  $R_2 = R_{1\rho}/\sin^2\theta - R_1/\tan^2\theta$ , where  $\theta = \arctan(\omega_1/\Omega)$  with  $\omega_1$  the spin-lock field and  $\Omega$  the  $^{15}\text{N}$  resonance offset. For fitting Lipari-Szabo models [72,73], we used ModelFree version 4.20 that was available in the NMRbox [74] virtual machine. The rotational correlation times ( $\tau_c$ ) were derived from analysis of the  $^{15}\text{N}$   $R_2/R_1$  ratios for residues that did not show evidence of significant ps-ns or  $\mu\text{s}$ -ms dynamics [75,76].

To estimate  $\tau_c$  from the  $R_2/R_1$  ratios and calculate the  $R_h$  for an assumed spherical particle, we used the following equations:

$$\tau_c \approx \frac{\sqrt{\frac{6T_1}{T_2} - 7}}{4\pi\nu_N} \quad (2)$$

$$R_h = \sqrt[3]{\frac{3Tk_B T_c}{4\pi\eta}} \quad (3)$$

Where  $\nu_N$  is the Larmor frequency of  $^{15}\text{N}$  (here 60.848 MHz),  $k_B$  is Boltzmann's constant, and  $\eta$  is the viscosity of water (1.1373 cP at 15  $^\circ\text{C}$ ). By substituting  $\tau_c$  into Eq. (3), we are able to obtain an estimate for the  $R_h$  of the particle with the assumption that the particle is spherical.

The  $^{15}\text{N}$  relaxation data at 600 and 900 MHz were fit to Lipari-Szabo models using ModelFree4.20 [77] within the NMRbox [74]. The length of the N–H bond vector was set to 1.02  $\text{\AA}$ , and the  $^{15}\text{N}$  CSA value was set at  $-160$  ppm. Since no high-resolution structure of the cHSP27 monomer is available, we fit its relaxation data, assuming an isotropic rotational diffusion tensor. A global rotational correlation time ( $\tau_c$ ) of  $6 \pm 0.8$  ns was determined from  $^{15}\text{N}$   $R_2/R_1$  ratios (Eq. (2)). Residues with evidence of ps-ns and  $\mu\text{s}$ -ms motions, as respectively determined by  $^{15}\text{N}\{^1\text{H}\}$  NOEs  $<0.65$  and  $R_2$  values greater than  $1.5\langle R_2 \rangle + 1$  standard deviation, were excluded from this analysis. Preliminary Lipari-Szabo modeling using global rotational correlation times within a range of 5–7 ns showed that the relaxation data from the interfacial region could not be adequately described alongside the rest of the molecule, even when including parameters to account for rapid internal motions ( $\tau_e$ ) on the picosecond timescale and exchange ( $R_{ex}$ ) contributions to  $R_2$ . Thus, we fit the data

using a local  $\tau_c$  for each residue that could vary between 1 and 7 ns, alongside a  $\tau_e$  parameter to account for more rapid motions faster than 100 ps and  $R_{ex}$  to account for exchange. Excluding the dynamic residues at the N-terminus (V85-R94) and the interfacial region (E125-S137), the average value of the locally fit  $\tau_c$  is  $5.89 \pm 0.80$  ns (Supplementary Fig. 4), which agrees well with the global  $\tau_c$  determined from  $R_2/R_1$  ratios. We note that  $R_{ex}$  terms were required at the dimer interface, suggesting that exchange may not have been fully suppressed by the 1 kHz spin lock. We fit the  $^{15}\text{N}$  relaxation data from the cHSP27 dimer to Lipari-Szabo models using an isotropic rotational diffusion tensor with  $\tau_c$  set to 12.5 ns.

### Residual dipolar couplings

$^1\text{H}$ – $^{15}\text{N}$  RDCs were recorded using gradient-enhanced IPAP-HSQC spectra [78] at 900 MHz under both isotropic and anisotropic conditions where scalar couplings ( $^1J_{\text{NH}}$ ) or scalar and dipolar couplings ( $^1J_{\text{NH}} + ^1D_{\text{NH}}$ ) are respectively active. Partial alignment of the cHSP27 dimer (0.78 mM) was achieved with preparation of a liquid crystalline 4.3% (v/v) mixture of C12E5 poly-ethylene-glycol (PEG)/hexanol [79] in buffer containing 30 mM sodium phosphate, 2 mM EDTA, and 6%  $\text{D}_2\text{O}$  at pH 7. Similar preparation of a 4.3% (v/v) PEG-hexanol liquid crystalline mixture was performed to align the cHSP27 monomer in the same buffer with a pH of 4.1. Both datasets were recorded at 25 °C. The couplings were calculated by measuring the difference in  $^{15}\text{N}$  chemical shifts in the IP/AP HSQC spectra, and then computing the difference in these values between aligned and unaligned samples. The negative sign associated with  $^1J_{\text{NH}}$  was ignored in these calculations.

The alignment tensor of the cHSP27 dimer was determined by singular value decomposition (SVD) fitting of couplings to the 2.6-Å crystal structure of the dimer (PDB: 4mjh) using the DC program from the NMRPipe package and the webserver for dipolar coupling analyses (<https://spin.niddk.nih.gov/bax/nmrserver/dc/>). Protons were added to the structure using the PDB Utility webserver (<https://spin.niddk.nih.gov/bax/nmrserver/pdbutil/sa.html>). Since the crystal structure of cHSP27 was co-crystallized with an eight-residue peptide bound between the  $\beta_4$  and  $\beta_8$  strands, we removed these chains (B, D) from the PDB file. To ensure accurate determination of the alignment tensor, only residues in well-structured regions of the dimer without evidence of exchange, as determined by previous measurements of  $^{15}\text{N}$  CPMG relaxation dispersion [26], were fit. These included residues in the  $\beta_3$  (V97, S98, L99, D100),  $\beta_4$  (V111, K112, T113, K114),  $\beta_8$  (S154, S155, L157, S158), and  $\beta_9$  (T162, T164, V165, E166, A167) strands, as well as residues in the rigid loop between  $\beta_6+7$  and  $\beta_8$  (Q152, V153), which collectively cover a large portion of the molecule. Due to the symmetric nature of the cHSP27 dimer, such that only one set of resonances is observed in its 2D  $^1\text{H}$ – $^{15}\text{N}$  HSQC spectrum, these 19 couplings were fit to  $2 \times 19$  N–H bond vectors in the crystal structure. From the fitted alignment tensor and the crystal structure, values of  $^1D_{\text{NH}}$  were calculated and compared to the remaining experimentally measured values. A similar procedure was

used to analyze RDCs measured for the cHSP27 monomer, except that the PDB structure entailed chain A from the crystal structure of the dimer (PDB: 4mjh). The same set of residues was used to fit the alignment tensor of the monomer, and both alignment tensors are reported in Table 2. For both sets of couplings, we calculated a Q factor [48] to assess the quality of the agreement between the experimentally measured RDCs and those predicted from the structures:

$$Q = \frac{\sqrt{\sum_i^n (\hat{D}_{\text{NH},i} - D_{\text{NH},i})^2}}{\sqrt{\sum_i^n \hat{D}_{\text{NH},i}^2}} \quad (4)$$

Where the summation includes the total number of residues with measured RDCs that are present in the crystal structure ( $i = 1, 2, 3, \dots, n$ ), and therefore enable a prediction. The accent atop the RDC notation,  $\hat{D}_{\text{NH},i}$ , indicates a measured value while its absence indicates a predicted value. The measured RDCs for both the dimer and monomer have been included as Table S1 in the Supporting Information.

### Disorder index

We obtained oligomers known to dissociate into disordered monomers from the Mutual Folding Induced Binding (MFIB) database [51], totaling 205 entries as of January 2020. Since the structures of ACDs are dimers, and to avoid potential bias introduced by the presence of more than one interface, we filtered the MFIB database to extract only dimers, which left 133 entries. Each dimer contains two subunits, and therefore our dataset contained a total of 266 monomer structures among the dimers that dissociate into disordered monomers. For the set of dimers that are not known to dissociate into disordered monomers, we used a curated set of 122 crystal structures in which no two sequences have more than 25% sequence identity, and the quaternary structure of the dimer in solution has been verified [80]. This set was used by the original authors to analyze homodimeric interfaces, and thus, the authors were not concerned if the dimers dissociated into ordered or disordered monomers. We therefore manually filtered the dataset to remove entries that are present in the MFIB database, contain evidence of a globally or locally unfolded monomer or metastable conformation, or fold in a two-state process without evidence for a stable monomeric intermediate. This left a total of 98 dimers or 196 monomer structures. For the set of sHSP structures, we download all available structures of sHSPs or their ACDs from the Protein Data Bank, totaling 39 structures or 78 monomer structures.

We computed structural properties for each complex using the Proteins, Interfaces, Structures, and Assemblies (PISA) interface and in-house Python scripts to facilitate automation [81]. Each complex was subjected to a PISA Interface analysis, which computes the SASA and BSA for each chain in the dimer. The disorder index is then computed by taking the ratio of the per-residue SASA and per-residue BSA, *i.e.*, the total SASA for a given chain divided by the total number of residues and the BSA

caused by complex formation divided by the total number of residues that comprise the interface. An in-house Python script was written to interface with the PISA webserver to access precalculated results for most of the complexes, which enabled the rapid calculation of structural properties. The raw data have been included as a downloadable file in the Supporting Information.

### Keywords:

NMR;  
Molecular chaperone;  
Small heat-shock protein;  
Conditional disorder;  
Residual dipolar couplings

## Acknowledgments

We thank James Baber and Yang Shen (NIH) for technical support. We are grateful to Iva Pritišanac (The Hospital for Sick Children, Toronto) for insightful comments and suggestions on the manuscript. This study made use of NMRbox: National Center for Biomolecular NMR Data Processing and Analysis, a Biomedical Technology Research Resource (BTRR), which is supported by NIH grant P41GM111135 (NIGMS). This work was supported by the Intramural Research Program of the NIDDK and by the Intramural Antiviral Target Program of the Office of the Director, NIH. T.R.A. acknowledges funding from the NIDDK and the NIH Oxford-Cambridge Scholars Program. A.J.B. holds a David Phillips Fellowship from the Biotechnology and Biosciences Research Council (BB/J014346/1). J.L.P.B. thanks the Engineering and Physical Sciences Research Council (EP/J01835X/1) and Biotechnology and Biosciences Research Council (BB/J018082/1).

## Author contributions

Conceptualization: T.R.A., A.B., J.L.P.B., and A.J.B. Investigation: T.R.A., J.Y., A.B., J.L.P.B., and A.J.B. Writing – Original Draft, T.R.A. Writing – Reviewing and Editing, T.R.A., J.Y., A.B., J.L.P.B., and A.J.B.

## Conflicts of interest

The authors declare no conflict of interest.

## Appendix A. Supplementary data

Supplementary data to this article can be found online at <https://doi.org/10.1016/j.jmb.2020.02.003>.

Received 30 October 2019;

Received in revised form 27 January 2020;

Accepted 9 February 2020

Available online 17 February 2020

## References

- [1] M. Haslbeck, S. Weinkauf, J. Buchner, Small heat shock proteins: simplicity meets complexity, *J. Biol. Chem.* 294 (2019) 2121–2132, <https://doi.org/10.1074/jbc.REV118.002809>.
- [2] H.H. Kampinga, R. de Boer, N. Beerstra, *The Multicolored World of the Human HSPB Family*, Springer International Publishing, Cham, 2015, <https://doi.org/10.1007/978-3-319-16077-1>.
- [3] A. Mogk, C. Ruger-Herreros, B. Bukau, Cellular functions and mechanisms of action of small heat shock proteins, *Annu. Rev. Microbiol.* 73 (2019), <https://doi.org/10.1146/annurev-micro-020518-115515> annurev-micro-020518-115515.
- [4] M.K. Janowska, H.E.R. Baughman, C.N. Woods, R.E. Klevit, Mechanisms of small heat shock proteins, *Cold Spring Harb. Perspect. Biol.* (2019), a034025, <https://doi.org/10.1101/cshperspect.a034025>.
- [5] A.P. Arrigo, HSP27: novel regulator of intracellular redox state, *IUBMB Life* 52 (2001) 303–307, <https://doi.org/10.1080/152165401317291165>.
- [6] D.R. Ciocca, S.K. Calderwood, Heat shock proteins in cancer: diagnostic, prognostic, predictive, and treatment implications, *Cell Stress Chaperones* 10 (2005) 86–103, <https://doi.org/10.1379/csc-99r.1>.
- [7] O. Straume, T. Shimamura, M.J.G. Lampa, J. Carretero, A.M. Øyan, D. Jia, C.L. Borgman, M. Soucheray, S.R. Downing, S.M. Short, S.-Y. Kang, S. Wang, L. Chen, K. Collett, I. Bachmann, K.-K. Wong, G.I. Shapiro, K.H. Kalland, J. Folkman, R.S. Watnick, L.A. Akslen, G.N. Naumov, Suppression of heat shock protein 27 induces long-term dormancy in human breast cancer, *Proc. Natl. Acad. Sci. U. S. A.* 109 (2012) 8699–8704, <https://doi.org/10.1073/pnas.1017909109>.
- [8] A.R. Clark, N.H. Lubsen, C. Slingsby, sHSP in the eye lens: crystallin mutations, cataract and proteostasis, *Int. J. Biochem. Cell Biol.* 44 (2012) 1687–1697, <https://doi.org/10.1016/j.biocel.2012.02.015>.
- [9] L.N. Makley, K.A. McMenimen, B.T. DeVree, J.W. Goldman, B.N. McGlasson, P. Rajagopal, B.M. Donyak, T.J. McQuade, A.D. Thompson, R. Sunahara, R.E. Klevit, U.P. Andley, J.E. Gestwicki, Pharmacological chaperone for  $\alpha$ -crystallin partially restores transparency in cataract models, *Science* 350 (2015) 674–677, <https://doi.org/10.1126/science.aac9145>, 80-.
- [10] J.M. Webster, A.L. Darling, V.N. Uversky, L.J. Blair, Small heat shock proteins, big impact on protein aggregation in neurodegenerative disease, *Front. Pharmacol.* 10 (2019) 1047, <https://doi.org/10.3389/fphar.2019.01047>.
- [11] E. Adriaenssens, T. Geuens, J. Baets, A. Echaniz-Laguna, V. Timmerman, Novel insights in the disease biology of mutant small heat shock proteins in neuromuscular dis-

- eases, *Brain* 140 (2017) 2541–2549, <https://doi.org/10.1093/brain/awx187>.
- [12] V.V. Nefedova, L.K. Muranova, M.V. Sudnitsyna, A.S. Ryzhavskaia, N.B. Gusev, Small heat shock proteins and distal hereditary neuropathies, *Biochemistry* 80 (2015) 1734–1747, <https://doi.org/10.1134/S000629791513009X>.
- [13] M. V. Sudnitsyna, E. V. Mymrikov, A.S. Seit-Nebi, N.B. Gusev, The role of intrinsically disordered regions in the structure and functioning of small heat shock proteins, *Curr. Protein Pept. Sci.* 13 (2012) 76–85, <https://doi.org/10.2174/138920312799277875>.
- [14] J.A. Carver, A.B. Grosas, H. Ecroyd, R.A. Quinlan, The functional roles of the unstructured N- and C-terminal regions in  $\alpha$ B-crystallin and other mammalian small heat-shock proteins, *Cell Stress Chaperones* 22 (2017) 627–638, <https://doi.org/10.1007/s12192-017-0789-6>.
- [15] C. Holt, J.K. Raynes, J.A. Carver, Sequence characteristics responsible for protein-protein interactions in the intrinsically disordered regions of caseins, amelogenins, and small heat-shock proteins, *Biopolymers* (2019), e23319, <https://doi.org/10.1002/bip.23319>.
- [16] H.E.R. Baughman, T.-H.T. Pham, C.S. Adams, A. Nath, R.E. Klevit, Release of a disordered domain enhances HspB1 chaperone activity toward tau, *Proc. Natl. Acad. Sci. Unit. States Am.* (2020), 201915099, <https://doi.org/10.1073/pnas.1915099117>.
- [17] G.R. Hilton, H. Lioe, F. Stengel, A.J. Baldwin, J.L.P. Benesch, Small heat-shock proteins: paramedics of the cell, *Top. Curr. Chem.* 328 (2013) 69–98, [https://doi.org/10.1007/128\\_2012\\_324](https://doi.org/10.1007/128_2012_324).
- [18] G.K.A. Hochberg, J.L.P. Benesch, Dynamical structure of  $\alpha$ B-crystallin, *Prog. Biophys. Mol. Biol.* 115 (2014) 11–20, <https://doi.org/10.1016/j.pbiomolbio.2014.03.003>.
- [19] J.L.P. Benesch, J.A. Aquilina, A.J. Baldwin, A. Rekas, F. Stengel, R.a. Lindner, E. Basha, G.L. Devlin, J. Horwitz, E. Vierling, J.a. Carver, C.V. Robinson, The quaternary organization and dynamics of the molecular chaperone HSP26 are thermally regulated, *Chem. Biol.* 17 (2010) 1008–1017, <https://doi.org/10.1016/j.chembiol.2010.06.016>.
- [20] T. Fleckenstein, A. Kastenmüller, M.L. Stein, C. Peters, M. Daake, M. Krause, D. Weinfurter, M. Haslbeck, S. Weinkauff, M. Groll, J. Buchner, The chaperone activity of the developmental small heat shock protein Sip1 is regulated by pH-dependent conformational changes, *Mol. Cell.* 58 (2015) 1067–1078, <https://doi.org/10.1016/j.molcel.2015.04.019>.
- [21] A.J. Baldwin, H. Lioe, C. V. Robinson, L.E. Kay, J.L.P. Benesch,  $\alpha$ B-crystallin polydispersity is a consequence of unbiased quaternary dynamics, *J. Mol. Biol.* 413 (2011) 297–309, <https://doi.org/10.1016/j.jmb.2011.07.016>.
- [22] W. Jiao, W. Hong, P. Li, S. Sun, J. Ma, M. Qian, M. Hu, Z. Chang, The dramatically increased chaperone activity of small heat-shock protein IbpB is retained for an extended period of time after the stress condition is removed, *Biochem. J.* 410 (2008) 63–70, <https://doi.org/10.1042/BJ20071120>.
- [23] C.J.O. Kaiser, C. Peters, P.W.N. Schmid, M. Stavropoulou, J. Zou, V. Dahiya, E.V. Mymrikov, B. Rockel, S. Asami, M. Haslbeck, J. Rappsilber, B. Reif, M. Zacharias, J. Buchner, S. Weinkauff, The structure and oxidation of the eye lens chaperone  $\alpha$ A-crystallin, *Nat. Struct. Mol. Biol.* 26 (2019) 1141–1150, <https://doi.org/10.1038/s41594-019-0332-9>.
- [24] B. Jovcevski, M.A. Kelly, A.P. Rote, T. Berg, H.Y. Gastall, J.L.P. Benesch, J.A. Aquilina, H. Ecroyd, Phosphomimics destabilize Hsp27 oligomeric assemblies and enhance chaperone activity, *Chem. Biol.* 22 (2015) 186–195, <https://doi.org/10.1016/j.chembiol.2015.01.001>.
- [25] A.F. Clouser, H.E. Baughman, B. Basanta, M. Guttman, A. Nath, R.E. Klevit, Interplay of disordered and ordered regions of a human small heat shock protein yields an ensemble of “quasi-ordered” states, *Elife* 8 (2019), <https://doi.org/10.7554/eLife.50259>.
- [26] T.R. Alderson, J. Roche, H.Y. Gastall, D.M. Dias, I. Pritišanac, J. Ying, A. Bax, J.L.P. Benesch, A.J. Baldwin, Local unfolding of the HSP27 monomer regulates chaperone activity, *Nat. Commun.* 10 (2019) 1–16, <https://doi.org/10.1038/s41467-019-08557-8>.
- [27] L. Almeida-Souza, S. Goethals, V. de Winter, I. Dierick, R. Gallardo, J. Van Durme, J. Irobi, J. Gettemans, F. Rousseau, J. Schymkowitz, V. Timmerman, S. Janssens, Increased monomerization of mutant HSPB1 leads to protein hyperactivity in charcot-marie-tooth neuropathy, *J. Biol. Chem.* 285 (2010) 12778–12786, <https://doi.org/10.1074/jbc.M109.082644>.
- [28] A.R. Clark, W. Vree Egberts, F.D.L. Kondrat, G.R. Hilton, N.J. Ray, A.R. Cole, J.A. Carver, J.L.P. Benesch, N.H. Keep, W.C. Boelens, C. Slingsby, Terminal regions confer plasticity to the tetrameric assembly of human HspB2 and HspB3, *J. Mol. Biol.* 430 (2018) 3297–3310, <https://doi.org/10.1016/j.jmb.2018.06.047>.
- [29] A.J. Baldwin, G.R. Hilton, H. Lioe, C. Bagnéris, J.L.P. Benesch, L.E. Kay, Quaternary dynamics of  $\alpha$ B-crystallin as a direct consequence of localised tertiary fluctuations in the C-terminus, *J. Mol. Biol.* 413 (2011) 310–320, <https://doi.org/10.1016/j.jmb.2011.07.017>.
- [30] A.R. Clark, C.E. Naylor, C. Bagnéris, N.H. Keep, C. Slingsby, Crystal structure of R120G disease mutant of human  $\alpha$ B-crystallin domain dimer shows closure of a groove, *J. Mol. Biol.* 408 (2011) 118–134, <https://doi.org/10.1016/j.jmb.2011.02.020>.
- [31] G.K.A. Hochberg, H. Ecroyd, C. Liu, D. Cox, D. Cascio, M.R. Sawaya, M.P. Collier, J. Stroud, J.A. Carver, A.J. Baldwin, C.V. Robinson, D.S. Eisenberg, J.L.P. Benesch, A. Laganowsky, The structured core domain of B-crystallin can prevent amyloid fibrillation and associated toxicity, *Proc. Natl. Acad. Sci. Unit. States Am.* 111 (2014) E1562–E1570, <https://doi.org/10.1073/pnas.1322673111>.
- [32] P. Rajagopal, Y. Liu, L. Shi, A.F. Clouser, R.E. Klevit, Structure of the  $\alpha$ -crystallin domain from the redox-sensitive chaperone, HSPB1, *J. Biomol. NMR* 63 (2015) 223–228, <https://doi.org/10.1007/s10858-015-9973-0>.
- [33] P. Rajagopal, E. Tse, A.J. Borst, S.P. Delbecq, L. Shi, D.R. Southworth, R.E. Klevit, A conserved histidine modulates HSPB5 structure to trigger chaperone activity in response to stress-related acidosis, *Elife* 4 (2015), <https://doi.org/10.7554/eLife.07304>.
- [34] D. Cox, E. Selig, M.D.W. Griffin, J.A. Carver, H. Ecroyd, Small heat-shock proteins prevent  $\alpha$ -synuclein aggregation via transient interactions and their efficacy is affected by the rate of aggregation, *J. Biol. Chem.* 291 (2016) 22618–22629, <https://doi.org/10.1074/jbc.M116.739250>.
- [35] T.R. Alderson, J.L.P. Benesch, A.J. Baldwin, Proline isomerization in the C-terminal region of HSP27, *Cell Stress Chaperones* (2017) 1–13, <https://doi.org/10.1007/s12192-017-0791-z>.

- [36] A.F. Clouser, R.E. Klevit, pH-dependent structural modulation is conserved in the human small heat shock protein HSBP1, *Cell Stress Chaperones* (2017) 1–7, <https://doi.org/10.1007/s12192-017-0783-z>.
- [37] J.A. Marsh, S.A. Teichmann, Relative solvent accessible surface area predicts protein conformational changes upon binding, *Structure* 19 (2011) 859–867, <https://doi.org/10.1016/j.str.2011.03.010>.
- [38] J.A. Marsh, Buried and accessible surface area control intrinsic protein flexibility, *J. Mol. Biol.* 425 (2013) 3250–3263, <https://doi.org/10.1016/j.jmb.2013.06.019>.
- [39] K. Gunasekaran, C.J. Tsai, R. Nussinov, Analysis of ordered and disordered protein complexes reveals structural features discriminating between stable and unstable monomers, *J. Mol. Biol.* 341 (2004) 1327–1341, <https://doi.org/10.1016/j.jmb.2004.07.002>.
- [40] T.R. Alderson, L.E. Kay, Unveiling invisible protein states with NMR spectroscopy, *Curr. Opin. Struct. Biol.* 60 (2020) 39–49, <https://doi.org/10.1016/j.sbi.2019.10.008>.
- [41] J.T. Nielsen, F.A.A. Mulder, POTENCI: prediction of temperature, neighbor and pH-corrected chemical shifts for intrinsically disordered proteins, *J. Biomol. NMR* 70 (2018) 141–165, <https://doi.org/10.1007/s10858-018-0166-5>.
- [42] Deborah K. Wilkins, Shaun B. Grimshaw, V. Receveur, Christopher M. Dobson, A. Jonathan, A. Jones, L.J. Smith, Hydrodynamic radii of native and denatured proteins measured by pulse field gradient NMR techniques†, *Biochemistry* 38 (1999) 16424–16431, <https://doi.org/10.1021/BI991765Q>.
- [43] A. Mainz, B. Bardiaux, F. Kuppler, G. Multhaup, I.C. Felli, R. Pierattelli, B. Reif, Structural and mechanistic implications of metal binding in the small heat-shock protein  $\alpha$ B-crystallin, *J. Biol. Chem.* 287 (2012) 1128–1138, <https://doi.org/10.1074/jbc.M111.309047>.
- [44] G. Lipari, A. Szabo, Model-free approach to the interpretation of nuclear magnetic resonance relaxation in macromolecules. 1. Theory and range of validity, *J. Am. Chem. Soc.* 104 (1982) 4546–4559, <https://doi.org/10.1021/ja00381a009>.
- [45] A. Bax, G. Kontaxis, N. Tjandra, Dipolar couplings in macromolecular structure determination, in: *Methods Enzymol*, Academic Press Inc., 2001, pp. 127–174, [https://doi.org/10.1016/S0076-6879\(01\)39313-8](https://doi.org/10.1016/S0076-6879(01)39313-8).
- [46] M. Ottiger, F. Delaglio, A. Bax, Measurement of J and dipolar couplings from simplified two-dimensional NMR spectra, *J. Magn. Reson.* 131 (1998) 373–378, <https://doi.org/10.1006/jmre.1998.1361>.
- [47] M. Zweckstetter, A. Bax, Evaluation of uncertainty in alignment tensors obtained from dipolar couplings, *J. Biomol. NMR* 23 (2002) 127–137, <https://doi.org/10.1023/A:1016316415261>.
- [48] G. Cornilescu, J.L. Marquardt, M. Ottiger, A. Bax, Validation of protein structure from anisotropic carbonyl chemical shifts in a dilute liquid crystalline phase, *J. Am. Chem. Soc.* 120 (1998) 6836–6837, <https://doi.org/10.1021/ja9812610>.
- [49] K. Chen, N. Tjandra, The use of residual dipolar coupling in studying proteins by NMR, *Top. Curr. Chem.* 326 (2012) 47–67, [https://doi.org/10.1007/128\\_2011\\_215](https://doi.org/10.1007/128_2011_215).
- [50] M.P. Collier, T.R. Alderson, C.P. de Villiers, D. Nicholls, H.Y. Gastall, T.M. Allison, M.T. Degiacomi, H. Jiang, G. Mlynek, D.O. Fürst, P.F.M. van der Ven, K. Djinicovic-Carugo, A.J. Baldwin, H. Watkins, K. Gehmlich, J.L.P. Benesch, HspB1 phosphorylation regulates its intramolecular dynamics and mechanosensitive molecular chaperone interaction with filamin C, *Sci. Adv.* 5 (2019), eaav8421, <https://doi.org/10.1126/sciadv.aav8421>.
- [51] E. Fichó, I. Reményi, I. Simon, B. Mészáros, MFIB: a repository of protein complexes with mutual folding induced by binding, *Bioinformatics* 33 (2017) 3682–3684, <https://doi.org/10.1093/bioinformatics/btx486>.
- [52] J.L. Silva, C.F. Silveira, A. Correia Júnior, L. Pontes, Dissociation of a native dimer to a molten globule monomer. Effects of pressure and dilution on the association equilibrium of arc repressor, *J. Mol. Biol.* 223 (1992) 545–555, <http://www.ncbi.nlm.nih.gov/pubmed/1738163>. (Accessed 19 October 2016).
- [53] C.W. Lee, M.A. Martinez-Yamout, H.J. Dyson, P.E. Wright, Structure of the p53 transactivation domain in complex with the nuclear receptor coactivator binding domain of CREB binding protein, *Biochemistry* 49 (2010) 9964–9971, <https://doi.org/10.1021/bi1012996>.
- [54] T.L. Tapley, J.L. Körnera, M.T. Barge, J. Hupfeld, J.A. Schauerer, A. Gafni, U. Jakob, J.C.A. Bardwell, Structural plasticity of an acid-activated chaperone allows promiscuous substrate binding, *Proc. Natl. Acad. Sci. U. S. A.* 106 (2009) 5557–5562, <https://doi.org/10.1073/pnas.0811811106>.
- [55] M. Uhlén, L. Fagerberg, B.M. Hallström, C. Lindskog, P. Oksvold, A. Mardinoglu, Å. Sivertsson, C. Kampf, E. Sjöstedt, A. Asplund, I.M. Olsson, K. Edlund, E. Lundberg, S. Navani, C.A.K. Szigartyo, J. Odeberg, D. Djureinovic, J.O. Takanen, S. Hober, T. Alm, P.H. Edqvist, H. Berling, H. Tegel, J. Mulder, J. Rockberg, P. Nilsson, J.M. Schwenk, M. Hamsten, K. Von Feilitzen, M. Forsberg, L. Persson, F. Johansson, M. Zwahlen, G. Von Heijne, J. Nielsen, F. Pontén, Tissue-based map of the human proteome, *Science* 80 (2015) 347, <https://doi.org/10.1126/science.1260419>.
- [56] J.C.A. Bardwell, U. Jakob, Conditional disorder in chaperone action, *Trends Biochem. Sci.* 37 (2012) 517–525, <https://doi.org/10.1016/j.tibs.2012.08.006>.
- [57] U. Jakob, R. Kriwacki, V.N. Uversky, Conditionally and transiently disordered proteins: awakening cryptic disorder to regulate protein function, *Chem. Rev.* 114 (2014) 6779–6805, <https://doi.org/10.1021/cr400459c>.
- [58] O. Suss, D. Reichmann, Protein plasticity underlines activation and function of ATP-independent chaperones, *Front. Mol. Biosci.* 2 (2015), <https://doi.org/10.3389/fmolb.2015.00043>.
- [59] E.T. McDonald, M. Bortolus, H.A. Koteiche, H.S. Mchaourab, Sequence, structure, and dynamic determinants of Hsp27 (HspB1) equilibrium dissociation are encoded by the N-terminal domain, *Biochemistry* 51 (2012) 1257–1268, <https://doi.org/10.1021/bi2017624>.
- [60] P. Koldewey, F. Stull, S. Horowitz, R. Martin, J.C.A. Bardwell, Forces driving chaperone action, *Cell* 166 (2016) 369–379, <https://doi.org/10.1016/j.cell.2016.05.054>.
- [61] J.G. Ghosh, M.R. Estrada, J.I. Clark, Interactive domains for chaperone activity in the small heat shock protein, human  $\alpha$ B crystallin, *Biochemistry* 44 (2005) 14854–14869, <https://doi.org/10.1021/bi0503910>.
- [62] I. Pritisanic, R.M. Vernon, A.M. Moses, J.D. Forman-Kay, Entropy and information within intrinsically disordered protein regions, *Entropy* 21 (2019) 662, <https://doi.org/10.3390/e21070662>.
- [63] I. Santhanagopalan, M.T. Degiacomi, D.A. Shepherd, G.K.A. Hochberg, J.L.P. Benesch, E. Vierling, It takes a dimer to tango: oligomeric small heat shock proteins

- dissociate to capture substrate, *J. Biol. Chem.* 293 (2018) 19511–19521, <https://doi.org/10.1074/jbc.RA118.005421>.
- [64] D.T. Jones, D. Cozzetto, DISOPRED3: precise disordered region predictions with annotated protein-binding activity, *Bioinformatics* 31 (2015) 857–863, <https://doi.org/10.1093/bioinformatics/btu744>.
- [65] F. Delaglio, S. Grzesiek, G.W. Vuister, G. Zhu, J. Pfeifer, A. Bax, NMRPipe: a multidimensional spectral processing system based on UNIX pipes, *J. Biomol. NMR* 6 (1995) 277–293. <http://www.ncbi.nlm.nih.gov/pubmed/8520220>. (Accessed 18 May 2016).
- [66] W. Lee, M. Tonelli, J.L. Markley, Nmrfam-Sparky, Enhanced software for biomolecular NMR spectroscopy, *Bioinformatics* 31 (2015) 1325–1327, <https://doi.org/10.1093/bioinformatics/btu830>.
- [67] P. Vallurupalli, D.F. Hansen, L.E. Kay, Structures of invisible, excited protein states by relaxation dispersion NMR spectroscopy, *Proc. Natl. Acad. Sci. Unit. States Am.* 105 (2008) 11766–11771, <https://doi.org/10.1073/pnas.0804221105>.
- [68] A.S. Maltsev, J. Ying, A. Bax, Deuterium isotope shifts for backbone <sup>1</sup>H, <sup>15</sup>N and <sup>13</sup>C nuclei in intrinsically disordered protein  $\alpha$ -synuclein, *J. Biomol. NMR* 54 (2012) 181–191, <https://doi.org/10.1007/s10858-012-9666-x>.
- [69] D.M. LeMaster, J.C. Laluppa, D.M. Kushlan, Differential deuterium isotope shifts and one-bond <sup>1</sup>H-<sup>13</sup>C scalar couplings in the conformational analysis of protein glycine residues, *J. Biomol. NMR* 4 (1994) 863–870, <https://doi.org/10.1007/bf00398415>.
- [70] J. Ying, F. Delaglio, D.A. Torchia, A. Bax, Sparse multi-dimensional iterative lineshape-enhanced (SMILE) reconstruction of both non-uniformly sampled and conventional NMR data, *J. Biomol. NMR* (2016), <https://doi.org/10.1007/s10858-016-0072-7>.
- [71] N.-A. Lakomek, J. Ying, A. Bax, Measurement of <sup>15</sup>N relaxation rates in perdeuterated proteins by TROSY-based methods, *J. Biomol. NMR* 53 (2012) 209–221, <https://doi.org/10.1007/s10858-012-9626-5>.
- [72] G. Lipari, A. Szabo, Model-free approach to the interpretation of nuclear magnetic resonance relaxation in macromolecules. 1. Theory and range of validity, *J. Am. Chem. Soc.* 104 (1982) 4546–4559, <https://doi.org/10.1021/ja00381a009>.
- [73] G.M. Clore, A. Szabo, A. Bax, L.E. Kay, P.C. Driscoll, A.M. Gronenborn, Deviations from the simple two-parameter model-free approach to the interpretation of nitrogen-15 nuclear magnetic relaxation of proteins, *J. Am. Chem. Soc.* 112 (1990) 4989–4991, <https://doi.org/10.1021/ja00168a070>.
- [74] M.W. Maciejewski, A.D. Schuyler, M.R. Gryk, I.I. Moraru, P.R. Romero, E.L. Ulrich, H.R. Eghbalnia, M. Livny, F. Delaglio, J.C. Hoch, NMRbox: a Resource for biomolecular NMR computation, *Biophys. J.* 112 (2017) 1529–1534, <https://doi.org/10.1016/j.bpj.2017.03.011>.
- [75] N. Tjandra, S.E. Feller, R.W. Pastor, A. Bax, Rotational diffusion anisotropy of human ubiquitin from <sup>15</sup>N NMR relaxation, *J. Am. Chem. Soc.* 117 (1995) 12562–12566, <https://doi.org/10.1021/ja00155a020>.
- [76] L.E. Kay, D.A. Torchia, A. Bax, Backbone dynamics of proteins as studied by <sup>15</sup>N inverse detected heteronuclear NMR spectroscopy: application to staphylococcal nuclease, *Biochemistry* 28 (1989) 8972–8979. <http://www.ncbi.nlm.nih.gov/pubmed/2690953>. (Accessed 15 August 2018).
- [77] A.M. Mandel, M. Akke, A.G. Palmer, Backbone dynamics of *Escherichia coli* ribonuclease HI: correlations with structure and function in an active enzyme, *J. Mol. Biol.* 246 (1995) 144–163. <http://www.ncbi.nlm.nih.gov/pubmed/7531772>. (Accessed 5 June 2016).
- [78] M. Ottiger, F. Delaglio, A. Bax, Measurement of J and dipolar couplings from simplified two-dimensional NMR spectra, *J. Magn. Reson.* 131 (1998) 373–378, <https://doi.org/10.1006/jmre.1998.1361>.
- [79] M. Rückert, G. Otting, Alignment of biological macromolecules in novel nonionic liquid crystalline media for NMR experiments, *J. Am. Chem. Soc.* 122 (2000) 7793–7797, <https://doi.org/10.1021/ja001068h>.
- [80] R.P. Bahadur, P. Chakrabarti, F. Rodier, J. Janin, Dissecting subunit interfaces in homodimeric proteins, *Proteins Struct. Funct. Genet.* 53 (2003) 708–719, <https://doi.org/10.1002/prot.10461>.
- [81] E. Krissinel, K. Henrick, Inference of macromolecular assemblies from crystalline state, *J. Mol. Biol.* 372 (2007) 774–797, <https://doi.org/10.1016/j.jmb.2007.05.022>.